Materials Today Bio 16 (2022) 100398

Contents lists available at ScienceDirect

Materials Today Bio

journal homepage: www.journals.elsevier.com/materials-today-bio

Visualization system based on hierarchical targeting for diagnosis and treatment of hepatocellular carcinoma

Shasha Shi [a,b,e], Huipu Li [c], Xi Zheng [d], Lin Lv [a], Shengtao Liao [a], Peng Lu [f], Maoxia Liu [g], Hongyun Zhao [a,b,**], Zhechuan Mei [a,*]

[a] Department of Gastroenterology, The Second Affiliated Hospital of Chongqing Medical University, Chongqing, 400010, PR China
[b] Chongqing Key Laboratory of Ultrasound Molecular Imaging, The Second Affiliated Hospital of Chongqing Medical University, Chongqing, 400016, PR China
[c] Department of Gastroenterology, Chongqing Hospital of Traditional Chinese Medicine, Chongqing, 400020, PR China
[d] Department of Gastroenterology, Chongqing University Cancer Hospital, Chongqing, 400030, PR China
[e] Department of Gastroenterology, The Third Hospital of Mianyang, Sichuan Mental Health Center, Mianyang, 621000, PR China
[f] Second Department of Geriatrics, The Third Hospital of Mianyang, Sichuan Mental Health Center, Mianyang, 621000, PR China
[g] Outpatient Department, Chongqing Emergency Medical Center, Chongqing University Central Hospital, Chongqing, 400030, PR China

ARTICLE INFO

Keywords:
Visual system
Hierarchical targeting
Magnet
Hepatocellular carcinoma

ABSTRACT

The accuracy and enrichment rate of targeted drugs largely determine the clinical diagnosis and treatment effect. Therefore, the accuracy and enrichment rate of targeted drugs should be improved. We designed a visual diagnosis and treatment system based on hierarchical targeting. It consists of multifunctional magnetic nanoparticles and a bio magnetic material. Bio-magnet mediated primary targeting can effectively improve the drug enrichment rate in the target tissue. SNF peptide/epithelial cell adhesion molecule antibody mediated targeting liver cancer stem cells (LCSCs) (secondary target) can improve the accuracy of the treatment and its outcomes. Low intensity focused ultrasound irradiation can explode nanoparticles around LCSCs, which can cause physical damage to cells. The combination of released interferon gamma and its receptor (tertiary target) can be used to initiate chemotherapy and immunotherapy. Using the optical properties of Fe_3O_4 and the phase transformation ability of perfluoropentane, the system can enhance photoacoustic and ultrasonic molecular imaging enabling diagnosis and treatment visualization. Targeting LCSCs can accurately provide physical, chemical, and immune treatment of Hepatocellular carcinoma, making the therapeutic effect more effective and thorough. This system may provide a new method for a more accurate visual diagnosis and treatment of tumors.

1. Introduction

Various diagnostic and treatment strategies have been developed for tumors in recent years [1–3]. However, the enrichment rate of drugs or contrast agents in the target region is poor owing to the complex environment of the human body [4], which makes it impossible to diagnose and treat tumors efficiently at the molecular level. The low drug enrichment rate and high drug resistance of tumor cells, especially the high drug resistance of cancer stem cells (CSCs), also decrease the efficiency of the clinical drug treatment [5,6]. Recently, targeted drug delivery has gained attention as an effective strategy for precision therapy [7–9]. New technologies such as salivary protein detection of tumors [10], as well as the application of various new biomaterials in diseases [11], have provided new directions for diagnosing and treating diseases. However, even if nanoparticles enter the body to escape capture by the macrophage system in circulation, the high interstitial pressure in the tumor region greatly hinders the aggregation and diffusion of nanoparticles, preventing them from entering deeper into the tumor tissue and limiting their application against tumors [12,13]. To solve the above problems, previous strategies to modify nanoparticles mainly focused on their direct and specific recognition of target cells [13,14]; however, the results were unsatisfactory because nanoparticles should be highly enriched in the target tissue first and then reach the target cells and target receptors in large quantities, i.e., they should be accurately graded and targeted to tissues (primary target), cells (secondary target), and receptors (tertiary target) (see Schemes 1 and 2).

* Corresponding author.
** Corresponding author. Department of Gastroenterology, The Second Affiliated Hospital of Chongqing Medical University, Chongqing, 400010, PR China..
E-mail addresses: 302148@hospital.cqmu.edu.cn (H. Zhao), meizhechuan@cqmu.edu.cn (Z. Mei).

https://doi.org/10.1016/j.mtbio.2022.100398
Received 5 July 2022; Received in revised form 7 August 2022; Accepted 8 August 2022
Available online 22 August 2022

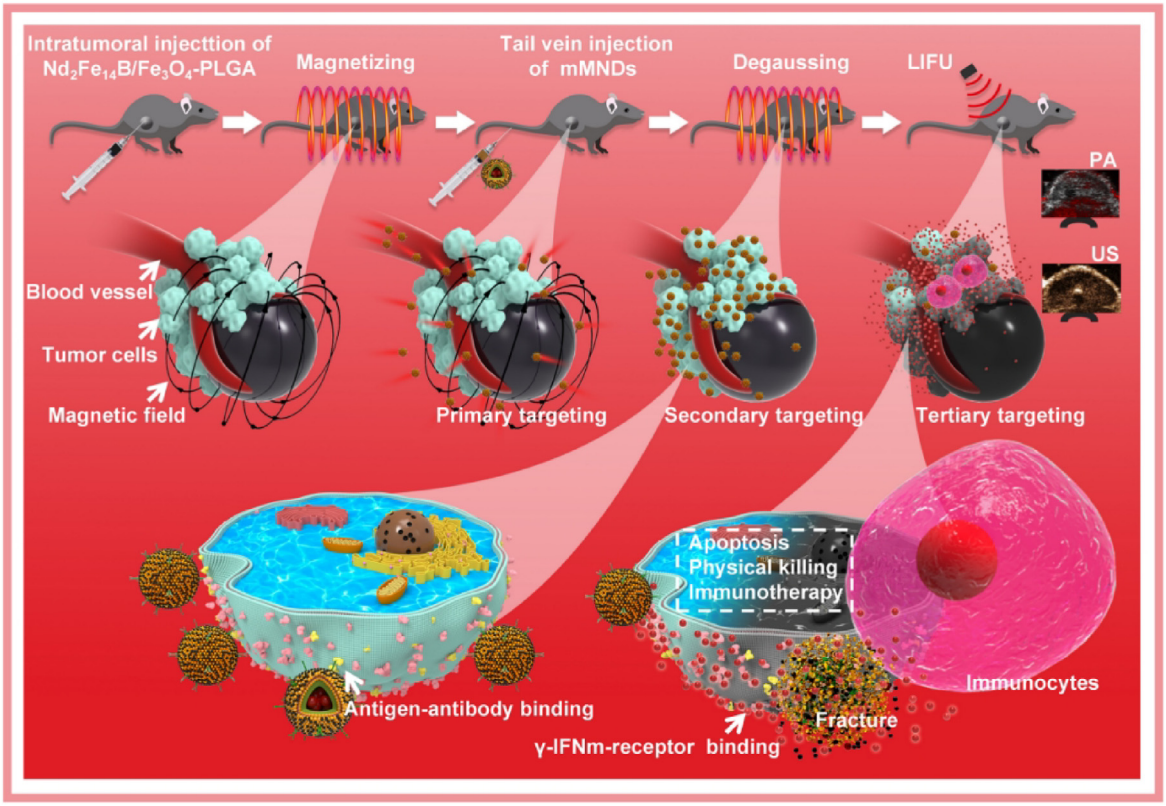

Scheme 1. Illustration to demonstrate the visualized diagnosis and treatment system based on hierarchical precision targeting and its therapeutic function involving multiple ways. Mice are magnetized after in a situ injection of $Nd_2Fe_{14}B/Fe_3O_4$-PLGA into the tumor. The magnetic field can attract a large number of magnetic nanoparticles into the deep tumor (primary target). After demagnetized, nanoparticles are released to targeting cells (secondary target). When nanoparticles are enriched around the target cells, they are irradiated by low intensity focused ultrasound. Gamma interferon is released from exploded nanoparticles and target receptors (tertiary target). This process produces chemotherapy, immunotherapy, and physical damage to the tumor.

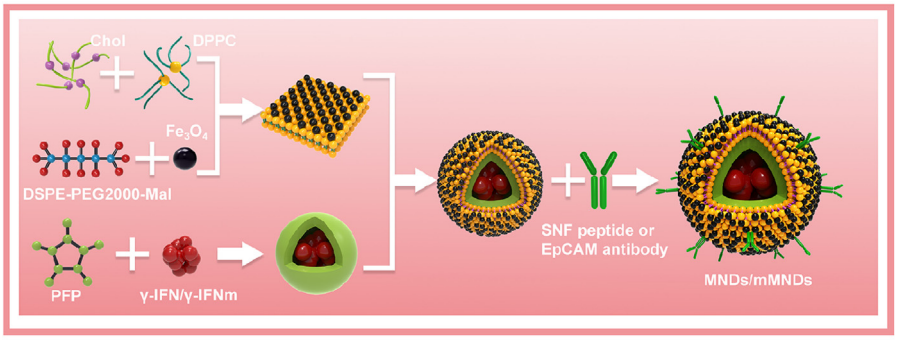

Scheme 2. Schematic illustration of synthesis of MNDs/mMNDs.

Some scholars have carried out magnetic targeting tests to improve the enrichment of nanoparticles in target tissues (primary targeting). They set a magnetic field *in vitro* to attract the circulating iron oxide to the tumor area [15–17]. However, with increasing *depth*, the strength of the magnetic field at the body surface decreases, causing more accumulation of nanoparticles at the skin tissue rather than deeper in the tumor tissue [18,19]. It has been shown that an injectable liquid-solid phase--transformation material *in vivo* may overcome these challenges [20]. We establish an *in vivo* magnetic field. Based on the property that the magnet can be magnetized and demagnetized [21], it is applied to improve the primary targeting ability of nanoparticles in the target tissue. When the nanoparticles in the bloodstream reach deep tumor locations following magnetic attraction, we demagnetize the magnetic force, which improves the nanoparticle enrichment rate in the tumor and does not affect the secondary and tertiary targeting of the nanoparticles. This facilitates uniform distribution of nanoparticles within the tumor, which in turn leads to a comprehensive and accurate visualization of the tumor for diagnosis and treatment. The Fe_3O_4 magnetic nanoparticles have an excellent light effect, which can enhance the photoacoustic imaging function. Simultaneously, liquid fluorocarbon phase change can enhance the ultrasound imaging function. These two are combined to achieve dual-modality imaging using ultrasound and photoacoustics [22–24].

While improving the enrichment rate of primary targeting, selecting important secondary molecular targets is crucial for therapeutic benefits. Most current targeted therapies only target typical tumor cells and ignore CSCs involved in tumorigenesis, progression, metastasis, and recurrence. CSCs are key factors contributing to the high rates of tumor recurrence, metastasis, and drug resistance [25,26]. Using CSCs with low

differentiation, rapid proliferation, and strong self-renewal abilities as secondary targets for drug delivery and treatment can help in eradicating tumors [27,28]. To improve the tumor cure rate and to reduce the recurrence and metastasis rates, the therapeutic strategy of targeting CSCs is needed further study. Epithelial cell adhesion molecule (EpCAM) is a membrane protein that is expressed in abnormally high quantities in hepatocellular carcinoma (HCC). It is also involved in the differentiation, proliferation, and migration of HCC cells. Furthermore, it is considered as a marker protein for liver cancer stem cells (LCSCs) [29]. Therefore, drug delivery programs targeting EpCAM are expected to eradicate the hotspots of HCC.

As a classical clinical drug, interferon gamma has targeting properties and can specifically bind to receptors on the surface of cell membranes to achieve final tertiary targeting [30]. Interferon gamma activates relevant pathways after binding to receptors on the membrane surface and enhances the expression of major histocompatibility complex (MHC) proteins while promoting apoptosis of tumor cells [31–34]. This is a combination of chemotherapy and immunotherapy. However, interferon gamma has a short half-life *in vivo* and toxic side effects. The use of nanoparticles as delivery carriers is a proven strategy for the safe and effective use of classical drugs [35,36].

In this study, we designed a visual diagnosis and treatment system based on hierarchical precise targeting. The system comprised of Fe_3O_4-γ–IFN–PFP-NPs:SNF (MNDs)/Fe_3O_4-γ-IFNm-PFP-NPs:EpC (mMNDs) and a bio-magnet. Magnetic nanoparticles combined with the optical properties of Fe_3O_4 and the liquid-gas phase transition ability of perfluoropentane can enhance the photoacoustic and ultrasonic molecular imaging functions. The bio-magnet-mediated nanoparticles were efficiently enriched in the primary target. The SNF peptide/EpCAM antibody screens target cells by binding to the secondary target EpCAM, and low intensity focused ultrasound irradiation causes physical damage to HCC cells by the phase change bursting of nanoparticles. It also upregulates the expression of MHC proteins while promoting apoptosis in HCC cells. Targeted LCSCs can precisely administer physical, chemical, and immune therapies (trinity treatment strategy) to LCSCs, making the therapeutic effect against HCC more effective and complete. Simultaneously, we conducted a more comprehensive and reliable validation in two different species of human-derived liver cancer models and murine liver cancer models. This system could be used as a new strategy for tumor visualization, diagnosis, and treatment; it improves the drug enrichment rate in target tissues and organs through primary targeting, increasing the accuracy of tumor visualization, diagnosis, and treatment through secondary and tertiary targeting.

2. Materials and methods

2.1. Materials and cells

Dipalmitoyl-phosphatidylcholine and cholesterol were purchased from Avanti (USA). The SNF peptides (sequence: SNFYMPLGGGSK) were synthesized by ChinaPeptides (Shanghai, China). DSPE-PEG2000-Mal was obtained from Xian Ruixi Biotechnology (Xi' an, China). Interferon gamma (human and mouse origin; purity: 95.0%) was purchased from T&L Biological Technology (Beijing, China). Fe_3O_4 was purchased from Ocean Technology Co., Ltd. (Springdale, AR, USA) and perfluoropentane (PFP) was purchased from Sigma-Aldrich (St. Louis, MO, USA). The Tris (2-carboxyethyl) phosphine hydrochloride (TCEP) was purchased from Beyotime Biotechnology (Shanghai, China). Polylactic-*co*-glycolic acid (PLGA, Mw: 40000 Da, 50:50) was purchased from Jinan Daigang Bioengineering Co. Ltd. (Jinan, China). N-methyl pyrrolidone was obtained from Sigma-Aldrich (AL, USA). Neodymium iron boron ($Nd_2Fe_{14}B$) particles (diameter: 30 μm) were obtained from Guangzhou Xinnuode Rotatable Part (Guangzhou, China). The Dioctadecyl-3,3,3′,3′-tetramethylindocarbocyanine (DiI) was obtained from Beyotime Biotechnology (Shanghai, China). 1,1′-dioctadecyl-3,3,3′,3′- tetramethylindotricarbocyanine iodide (DiR), calcein green-AM/propidium iodide PI and diamidino-phenylindole (DAPI) were obtained from Sigma-Aldrich (St. Louis, MO, USA). Dulbecco's modified Eagle's medium and fetal bovine serum were purchased from Gibco (Carlsbad, USA). Enzyme-linked immunosorbent assay (ELISA) kits were purchased from Meimian Industrial Co. Ltd. (Jiangsu, China). A Cell Counting Kit 8 (CCK-8) was provided by Dojindo Technology (Tokyo, Japan). N-methyl pyrrolidone (NMP) solvent were purchased from Sigma (Darmstadt, Germany). All the cell lines were purchased from Procell Life Science&Technology Co., Ltd. (Wuhan, China).

2.2. Synthesis of MNDs/mMNDs

To thoroughly validate the system's functionality, experiments were performed on two kinds of liver cancer models, human-derived and murine-derived. Thus, we designed Fe_3O_4-γ–IFN–PFP-NPs:SNF (MNDs) and Fe_3O_4-γ-IFNm-PFP-NPs:EpC (mMNDs) nanoparticles that corresponded to the different species. The MNDs were loaded with human-derived gamma interferon (γ-IFN) and SNF peptides [37], which were used to target human-derived EpCAM. The mMNDs were loaded with murine-derived gamma interferon (γ-IFNm) and murine-derived EpCAM antibodies.

Nanocarriers were synthesized following the previously reported thin-film hydration method and phacoemulsification method [38]. First, DPPC 5 mg, DSPE-PEG2000-Mal 2 mg, cholesterol 1 mg, and 20 μL Fe_3O_4 were added to a round-bottom flask and dissolved in 5 mL trichloromethane. The round-bottom flask was connected to a rotary evaporator and evaporated for 1 h at 52 °C. After dissolving 1 μg of γ-IFN/γ-IFNm in water, 200 μL PFP was added, which was first emulsified with an ultrasonic sonicator at 100 W (5 s on, 5 s off) for 3 min, and then all products were emulsified at the same power for 8 min. Then Fe_3O_4-γ–IFN–PFP-NPs/Fe_3O_4-γ-IFNm-PFP-NPs were prepared. SNF peptide/EpCAM antibody solution activated for 2 h with TCEP was then added. Next, the solution was placed in the refrigerator at 4°C overnight. Finally, MNDs/mMNDs were purified by centrifugation at 5000 rpm for 5 min at 4 °C. The supernatant was discarded and resuspended thrice in 3 mL of phosphate-buffered saline solution. Other nanocarrier solutions (Fe_3O_4-PFP-NPs:SNF, Fe_3O_4-γ–IFN–PFP-NPs, Fe_3O_4-PFP-NPs:EpC, and Fe_3O_4-γ-IFNm-PFP-NPs) were also fabricated using a similar method; except that γ-IFN/γ-IFNm, SNF peptides/EpCAM antibodies were added during the process. Fluorescently labeled MNDs/mMNDs were prepared by adding the corresponding markers (DiI and DiR) in the first step.

2.3. Synthesis of liquid $Nd_2Fe_{14}B/Fe_3O_4$-PLGA

PLGA (1.1 g) and NMP (2 mL) were placed into a bottle as past exploration [39]. To generate a homogenous PLGA liquid bio-injection, the PLGA was completely dissolved in NMP overnight at 37 °C, 120 r/min. Certain amount of $Nd_2Fe_{14}B$ and Fe_3O_4 particles were dispersed into PLGA liquid gel, and there are 0.38 g of $Nd_2Fe_{14}B$ and 0.15 g of Fe_3O_4 per ml of gel.

2.4. Characterization of MNDs/mMNDs

The MNDs/mMNDs were observed using transmission electron microscopy (Hitachi H-7600; Japan) and laser confocal microscopy (CLSM) (Nikon A1, Japan). A dynamic light scattering (DLS) detector (ZEN3600; Malvern Instruments, U.K.) was used to determine the diameter and zeta potential of MNDs/mMNDs. Notably, the mean sizes of MNDs/mMNDs were recorded at different time points (1, 2, 3, 7, and 14 days). Inductively coupled plasma optical emission spectrometry (ICP-OES; PerkinElmer 8300; USA) was used to measure the content of Fe_3O_4 loaded into the MNDs/mMNDs. The method for measuring the encapsulation rate and drug loading of the prepared MNDs/mMNDs was consistent with those used in previous reports; however, the method for testing drug concentration was replaced with the use of an ELISA kit. The shell was labeled with DiI and the SNF polypeptide/EpCAM antibody was labeled

with FITC. The dilution concentration of MNDs/mMNDs was adjusted to 50 mg/mL. The connection rate between the liposome shell and the SNF peptide/EpCAM antibody in MNDs/mMNDs was observed using CLSM and detected using flow cytometry (FC) (BD Biosciences, USA).

To study the acoustic phase transition, low intensity focused ultrasound (LIFU) (LMSC051ACA; Institute of Ultrasound Imaging, Chongqing Medical Sciences, Chongqing, China) was turned on, and the parameters were adjusted to pulse mode (2 s: on, 2 s: off). The MNDs/mMNDs were loaded into a 5 mL EP tube, placed at the center of the LIFU probe, irradiated with a focal length of 1.5 cm with different powers (1, 2, 3, 4 W/cm^2), and the MNDs/mMNDs were aspirated and dropped on a glass slide after 5 min of irradiation and placed under a light microscope for observation. LIFU drug release experiments were performed as described above using an original concentration of MNDs/mMNDs, and the drug concentration was calculated using an ELISA kit.

Nanoscale liposomes enhance the ultrasound (US) imaging capability when transformed to micron-scale or even larger sizes [40]. We used the parameters of the LIFU release drug experiment for the experiment of US imaging capability, and the MNDs/mMNDs after different treatments were observed using ultrasound diagnostic system (Mylab 90, Esaote, Italy); the image grayscale was analyzed using DFY software (Chongqing Medical University, China).

2.5. Safety of MND/mMND

All the animal experiments were approved by the Animal Ethics Committee of Chongqing Medical University and Institutional Animal Care.

The CCK-8 assay was used to detect the cytotoxicity of MNDs to Huh7 and mMNDs to Hepa1-6. The specific method was the same as the previous study [38].

To evaluate the *in vivo* biosafety of these mMNDs, healthy C57 mice were intravenously administered an mMNDs suspension (3 mg/mL, 200 μL per mouse). The shell was labeled with DiI and the EpCAM antibody was labeled with FITC. Mouse urine was smeared before injection and 2 h, 6 h, 24 h, and 48 h after injection (n = 3); it was observed under a fluorescence microscope (Olympus, Japan).

Mice were sacrificed before and 1, 2, and 7 days after the injection (n = 3), and blood samples were collected for serum iron, serum ferritin, hematology, and serum biochemical tests, respectively. The major organs (heart, liver, spleen, lung, and kidney) were subjected to autofluorescence detection, Prussian blue (PB), and Hematoxylin-eosin (H&E) staining on day 2.

2.6. Characterization of $Nd_2Fe_{14}B/Fe_3O_4$-PLGA

To study the liquid-solid phase change properties of $Nd_2Fe_{14}B/Fe_3O_4$-PLGA, the $Nd_2Fe_{14}B/Fe_3O_4$-PLGA liquid injection was loaded into a standard 1 mL syringe and injected into saline. The liquid $Nd_2Fe_{14}B/Fe_3O_4$-PLGA transformed into a solid form after contact with water. The prepared liquid $Nd_2Fe_{14}B/Fe_3O_4$-PLGA injection was injected into the skin of healthy C57 mice (n = 3). The phase-transformation procedure was dynamically guided by an US diagnostic system that captured US images every 30 s.

The $Nd_2Fe_{14}B/Fe_3O_4$-PLGA was charged using a magnetizing apparatus provided by the Chongqing University of Science and Technology, and turn into the bio-magnet. The magnetizer (MT-4060) had an 8-T center field strength, a peak charging voltage of DC 2000 V, and a peak electric field of 10,000 A. Before magnetization, after magnetization, and after demagnetization, the cured $Nd_2Fe_{14}B/Fe_3O_4$-PLGA was placed in Fe_3O_4 powder to investigate the magnetic absorption range and magnetic lines of force of the bio-magnet. A tesla meter was used to measure the magnetic force of the bio-magnet.

2.7. Safety of $Nd_2Fe_{14}B/Fe_3O_4$-PLGA

The CCK-8 assay was used to detect the cytotoxicity of $Nd_2Fe_{14}B/Fe_3O_4$-PLGA. The specific method was the same as the previous study [38].

The prepared liquid $Nd_2Fe_{14}B/Fe_3O_4$-PLGA bio injection was directly injected into the skin of healthy C57 mice. After curing, the size of the material was measured and recorded immediately after injection and at 1 and 2 months along with the weight of the loaded mice (n = 3). Mice were sacrificed before and 3, 7, 30, and 60 days after the injection (n = 3). Blood samples were collected for serum iron, serum ferritin, hematology, and biochemical tests. After degradation of the material, the remaining mice were euthanized. The major organs (heart, liver, spleen, lung, and kidney) were subjected to PB and H&E staining.

2.8. Cell culture and establishment of an animal xenograft model

Cells were adherently cultured with DMEM complete medium (10% fetal bovine serum). The cells were all cultured in a cell incubator at 37 °C, 5% CO_2, and 95% humidity and passaged or frozen when the cells were in the logarithmic phase. C57 mice (male, 4–5 weeks) were purchased from the Animal Experiment Center of Chongqing Medical University, housed in SPF-grade cages. Hepa1-6 cells were cultured until the logarithmic growth phase, the cell concentration was adjusted to 5–6 × 10^6/mL, and 200 μL of cells was subcutaneously injected into the root of the leg of each mouse. After approximately 15 days, the subcutaneous tumor was around 100 mm^3 in size. Due to its high fl uidity, the as-formed liquid $Nd_2Fe_{14}B/Fe_3O_4$-PLGA (25μL) can be immediately in-situ injected into tumors under ultrasound guidance. The NMP can swiftly diffuse into the surrounding aquatic environment after contacting the aqueous environment of tumor tissues. After placing the mice in the magnetizer for magnetization, the animal xenograft models with bio-magnets were prepared.

2.9. Cell line screening and EpCAM expression assay

Western blot (WB) was used to verify the expression of EpCAM in human and murine-derived cell lines, and the expression rate of EpCAM in selected cell lines was quantified using FC.

2.10. Secondary and tertiary targeting efficiency of MNDs/mMNDs in vitro

The method used to examine the efficacy of secondary targeting *in vitro* was same as that used in our previous reports [38]. We chose Huh7 and L02 cells to simulate human-derived tests and Hepa 1–6 and AML12 to simulate murine-derived tests. The FC detection method was the same as that reported previously.

To understand the secondary and tertiary targeting properties of the nanoparticles, we used the same approach as described above for the experiments. But after 1 h of nanoparticle addition to the culture dish, the LIFU was switched on. The parameter was adjusted as per the pulse mode (2 s: on, 2 s: off), and the power was 4 W/cm^2. The dish was placed at the center of the LIFU probe, irradiated with a focal length of 1.5 cm for 5 min, and placed in a cell incubator again for 1 h.

2.11. The therapeutic capability of MNDs in vitro

The concentration of Huh7 cells was adjusted to 5 × 10^6/mL; they were placed in a cell incubator until they completely adhered to the walls of the dish. The cells were divided into the following groups: 1, control; 2, LIFU; 3, Fe_3O_4-γ–IFN–PFP-NPs + LIFU; 4, MNDs + LIFU; 5, Fe_3O_4-PFP-NPs:SNF; 6, Fe_3O_4-PFP-NPs:SNF + LIFU; 7, Fe_3O_4-γ–IFN–PFP-NPs; 8, MNDs. Nanoparticles prepared in a serum-free medium were added and

placed in an incubator (the control group contained only serum-free medium). The LIFU-treated group was irradiated at 4 W/cm^2 for 5 min after 1 h of nanoparticles addition. Following 24 h of incubation, the liquid in the dish was removed and the cells were washed thrice with PBS. The expression of HLA-I was verified using WB and FC analyses.

The killing ability of the nanoparticles was detected using double staining with calcein green-AM/propidium iodide and FC. The specific method used was the same as that in our previous report [38].

2.12. Visualization and accurate targeting of mMNDs + Bio-magnet in vivo

To validate the primary targeting ability of the mMNDs + Bio-magnet system *in vivo*, tumor-bearing C57 mice were prepared. The fluorescent probe DIR was used to label the mMNDs. The mice were divided into mMNDs and mMNDs + Bio-magnet groups (n = 3), after they were subjected to gas anesthesia. First, the pre-images were collected using a NIRF imaging system (Xenogen IVIS Spectrum, PerkinElmer, U.K.); the mMNDs were injected from the tail vein (200 μL per mouse). Mice were placed in a fluorescence operating console, and fluorescence images were collected at 3, 12, and 24 h. After the mice were sacrificed, their viscera and tumors were separated and fluorescence images were collected. Finally, the corresponding fluorescence intensities were analyzed using Living Image Software (PerkinElmer).

Photoacoustic (PA) imaging of the mMNDs was first performed using full-band scanning with a wavelength of 680–970 nm, and the wavelength with the strongest PA signal (705 nm) was selected as the experimental wavelength. The mMNDs were diluted to different concentrations and injected into gel model holes. The intensities of the acquired PA images were measured using a PA imager. To perform mMNDs + bio-magnet system primary targeting ability *in vivo* using PA imaging, subcutaneous xenografts were constructed. Tumor-bearing C57 mice were divided into mMNDs and mMNDs + Bio-magnet groups (n = 3), after they were subjected to gas anesthesia. Pre-images without mMNDs were collected; the mMNDs were injected into the mice from the tail vein (200 μL per mouse). The PA images of the two groups were collected and analyzed for PA intensity at 1, 3, 12, and 24 h after the injection using Vevo LAZR software (VisualSonics Inc., Toronto, Canada).

The tumor-bearing C57 mice were divided into mMNDs and mMNDs + bio-magnet groups (n = 3). The two groups were subjected to different irradiation time using LIFU (pulse mode, 2 s: on, 2 s: off, 4 W/cm^2). The US images were obtained using the US diagnostic system in B-mode and contrast-enhanced ultrasound (CEUS), and the intensities were recorded via the DFY-texture (Chongqing Medical University, China). For more objective evaluation, the time-point of the highest mMNDs enrichment in each group for LIFU irradiation was selected based on the results of *in vivo* fluorescence and PA imaging experiments. The time-point of the mMNDs group was 12 h post-injection and that of the mMNDs + Bio-magnet group was 3 h post-injection.

In the above experiments, the mMNDs + bio-magnet group was subjected to demagnetization treatment 3 h following the mMNDs injection.

To study secondary and tertiary targeting from a microscopic perspective, tumor-bearing C57 mice were divided into mMNDs and mMNDs + bio-magnet groups (n = 3). DiI-labeled mMNDs loaded with FITC-labeled γ-IFNm were injected into the tail vein (200 μL per mouse). The time-point of the mMNDs group was 12 h post-injection and that of the mMNDs + Bio-magnet group was 3 h post-injection. The two groups were subjected to different irradiation time using LIFU (pulse mode, 2 s: on, 2 s: off, 4 W/cm^2, 15 min). Mice were sacrificed after irradiation. The tumor tissues were removed for sectioning, DAPI-stained nuclei were stained, and CLSM was used to observe the aggregation trend and the secondary and tertiary targeting performance of the mMNDs.

When the tissues were sectioned, the central part of the tumor tissue was selected for the mMNDs group. The tissues around the bio-magnet were selected for the mMNDs + bio-magnet group.

2.13. Therapeutic efficacy of mMNDs in vivo

Tumor-bearing C57 mice were divided into the following groups (n = 6): 1, control; 2, saline + LIFU; 3, mMNDs; 4, mMNDs + LIFU; 5, mMNDs + Bio-magnet; 6, mMNDs + Bio-magnet + LIFU; 7, Fe_3O_4-PFP-NPs:EpC + Bio-magnet + LIFU; 8, Fe_3O_4-γ-IFNm-PFP-NPs + Bio-magnet + LIFU. They were administered 200 μL of the corresponding nanoparticle solution through tail vein injection, and the control group was administered saline injection. LIFU irradiation (pulse mode, 2 s: on, 2 s: off, 4 W/cm^2, 15 min) was started 4 h after the injection once a day for 3 days. Changes in the body weight and tumor volume were recorded for 16 days. The bio magnetic precursor $Nd_2Fe_{14}B/Fe_3O_4$-PLGA was injected into the left tumor only, and the LIFU irradiated the same tumor. Groups with $Nd_2Fe_{14}B/Fe_3O_4$-PLGA, magnetization was given before tail vein injection and demagnetization was given 3 h after injection.

On day 3 after the end of treatment, the left tumors were harvested for immunofluorescence staining to study the expression of H-2 in tumor tissues. Additionally, the harvested left tumor was used to produce a single-cell suspension. The prepared cells were stained with H-2-FITC (BioLegend, USA) antibodies and analyzed using FC.

After understanding the effects of mMNDs on the immune microenvironment, we validated the tumor-killing ability of mMNDs. Tumor-bearing C57 mice were divided into the same treatment groups (n = 6), as described above. On day 3 after the end of treatment, the left tumor was harvested for TUNEL staining and a single-cell suspension was prepared for detecting apoptosis using FC.

During the treatment period, we recorded the left tumor size and weight of the tumor-bearing mice.

2.14. Statistical analysis

All results were presented as mean ± standard (mean ± SD). Statistical analyses were completed with Prism GraphPad. Unpaired Student's t-test (for two groups), one-way or two-way ANOVA (for multiple groups) were used followed by the Tukey-Kramer test (*$p < 0.05$ was considered statistically significant, **$p < 0.01$, ***$p < 0.001$, ****$p < 0.0001$).

3. Results and discussion

3.1. Preparation and characterization of MNDs and mMNDs

3.1.1. General characterization of MNDs and mMNDs

Low-magnification TEM and CLSM images revealed the successful synthesis of MNDs and mMNDs, both of which exhibited relatively uniform particle sizes and spherical states and good dispersion (Fig. 1A and E). High-magnification TEM showed that Fe_3O_4 in MNDs and mMNDs was well encapsulated in the core-shell and exhibited small black particles (Fig. 1A). DLS detected the average hydrodynamic diameters of MNDs and mMNDs as 321.91 ± 2.80 nm and 353.57 ± 7.43 nm (Fig. 1B). The zata potentials were −40.59 ± 1.56 mV and −40.55 ± 1.51 mV, respectively (Fig. 1I). After monitoring the 14-day particle size variation of MNDs and mMNDs (Fig. 1F), the results showed that the maximum particle sizes of the adopted core shells were 336.93 ± 3.55 nm and 384.50 ± 10.38 nm, respectively, demonstrating good stability of the nanoparticles. The inductively coupled plasma spectrometer detection of Fe loading revealed that the loading of Fe_3O_4 increased with increasing Fe_3O_4 addition, while the encapsulation rate decreased (Fig. 1C). The ELISA test suggested that the loading of γ-IFN and γ-IFNm similarly increased with drug addition. However, the encapsulation rate decreased gradually (Fig. 1D). Combining the loading and encapsulation rate analyses, the final selection of the nanoparticles was 20 μL of Fe_3O_4 and 1 μg of γ-IFNm. Our shell nuclei contain maleimide, which is often coupled with sulfhydryl groups on proteins to achieve selective modification. The Michael addition reaction is selective and rapid. The required reaction conditions is mild and simple. Several FDA-approved antibody-drug adducts have been clinically obtained using such reactions [41,42].

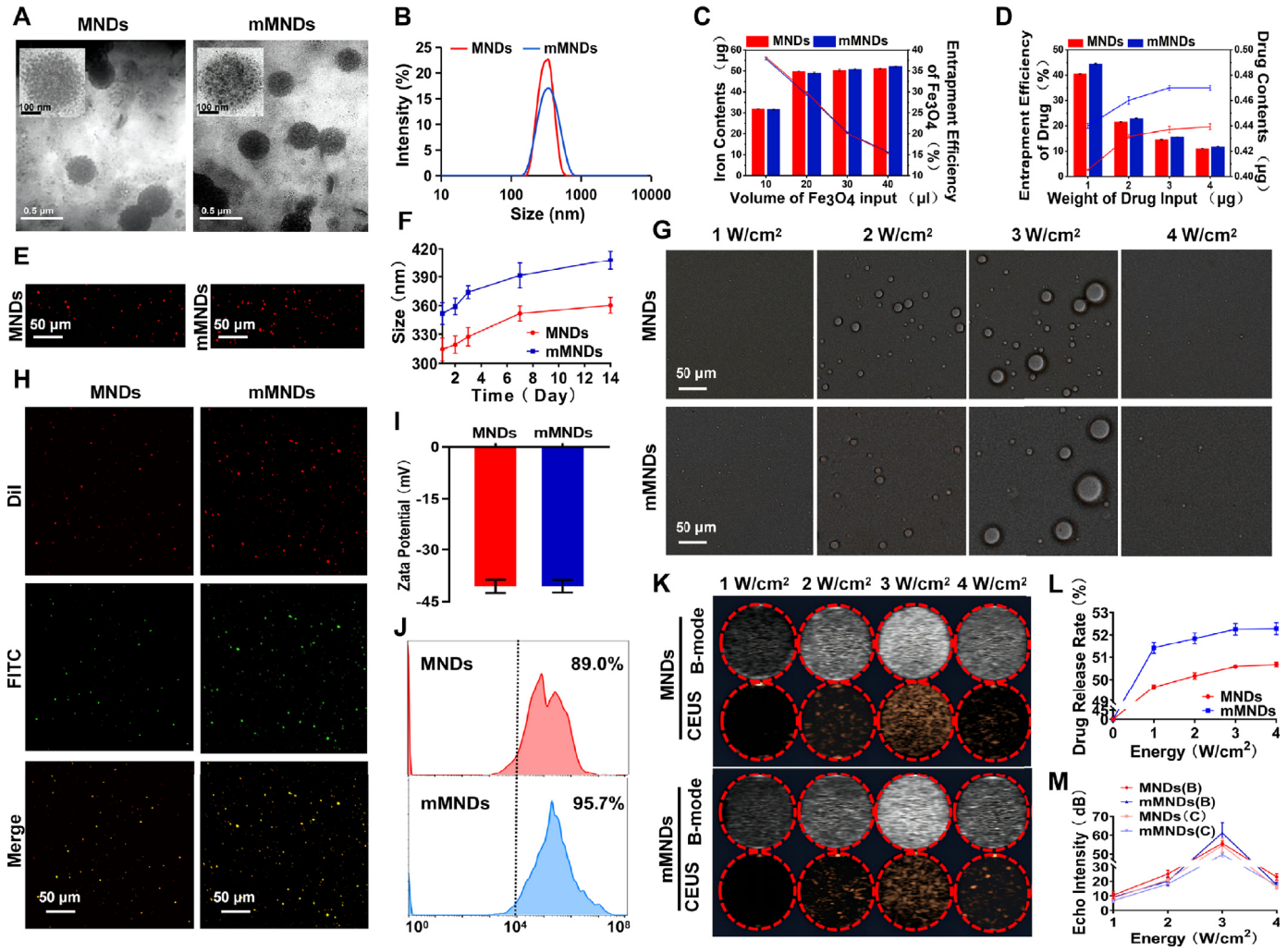

Fig. 1. Characterization of MNDs and mMNDs. A **Low and high magnification TEM images of MNDs and mMNDs.** B **Diameters of MNDs and mMNDs.** C **Concentrations and encapsulation efficiency of Fe3O4 from ICP-OES.** D **Concentrations and encapsulation efficiency of drug from ELISA.** E **CLSM images of MNDs and mMNDs.** F **Stability of MNDs and mMNDs based on DLS.** G **Phase transition of MNDs and mMNDs after LIFU irradiation with different power.** H&J **CLSM and FC to evaluate binding of SNF peptides/EpCAM antibodies and the shell of nanoparticles *in vitro*.** I **Zeta potentials of MNDs and mMNDs.** K **US images of MNDs and mMNDs after LIFU irradiation with different power.** L **Dug release curves from MNDs and mMNDs after LIFU irradiation with different power.** M **Average echo intensity values of US images, (B) means echo intensity values of B-mode and (C) means echo intensity values of CEUS-mode.**

Therefore, the Michael addition reaction is used in this study to attach the SNF peptide/EpCAM antibody to the corresponding nanoparticle shell and observed using CLSM. The DiI-labeled shells overlapped with the SNF peptides/EpCAM antibodies labeled with FITC and were orange in color. Quantitative analysis of the nanoparticle Michael addition reaction using FC showed that the attachment rate of nanoparticles to peptides was 89% and that to antibodies was 95.7% (Fig. 1H). SNF peptides/EpCAM antibodies are important components of secondary targeting in this system, and their efficient attachment to nanoparticles provides a good basis for secondary active targeting.

3.1.2. *Phase transition and drug release of MNDs and mMNDs*

The controlled release of the drug is significant for its therapeutic efficacy and biosafety, and the controlled phase changeability of PFP under LIFU irradiation has also been verified in a large number of experiments [40,43]. The phase changeability of the nanoparticles showed significant energy dependence under the same LIFU irradiation time (Fig. 1G). The same energy dependence of drug release was observed, up to 50.67% (MNDs) and 52.28% (MNDs) at 4 W/cm^2 (Fig. 1L). The same pattern of nanoparticle phase transition induced by LIFU irradiation was confirmed using *in vitro* US imaging (Fig. 1K). The average sound intensity peaked at 3 W/cm^2 and decreased as the nanoparticles broke down owing to the high energy (Fig. 1M). Thus, PFP responds efficiently to LIFU irradiation and can be used for precise and controlled drug release.

Therefore, efficient and straightforward synthesis of MNDs and mMNDs is crucial for future clinical conversion. Moreover, the results show that MNDs and mMNDs successfully encapsulate Fe_3O_4 and Gamma interferon; considering their nanoscale particle size and good liquid-gas phase transition properties, MNDs and mMNDs have the potential to guide visual grading and precision therapy.

3.2. *Metabolism and biosafety of mMNDs*

Metabolic pathways and biosafety are crucial for the clinical translation of novel drugs and biomaterials [44,45]. *In vitro* cytotoxicity test, there was no significant difference in cell survival rate between the experimental group and the control group, which preliminarily showed that MNDs/mMNDs had the good safety (Fig. 2B). *In vivo* experiments were mainly performed with mMNDs; thus, we focused on examining various effects of mMNDs on living organisms. The mMND shells were labeled with DiI, the EpCAM antibodies were labeled with FITC, and the

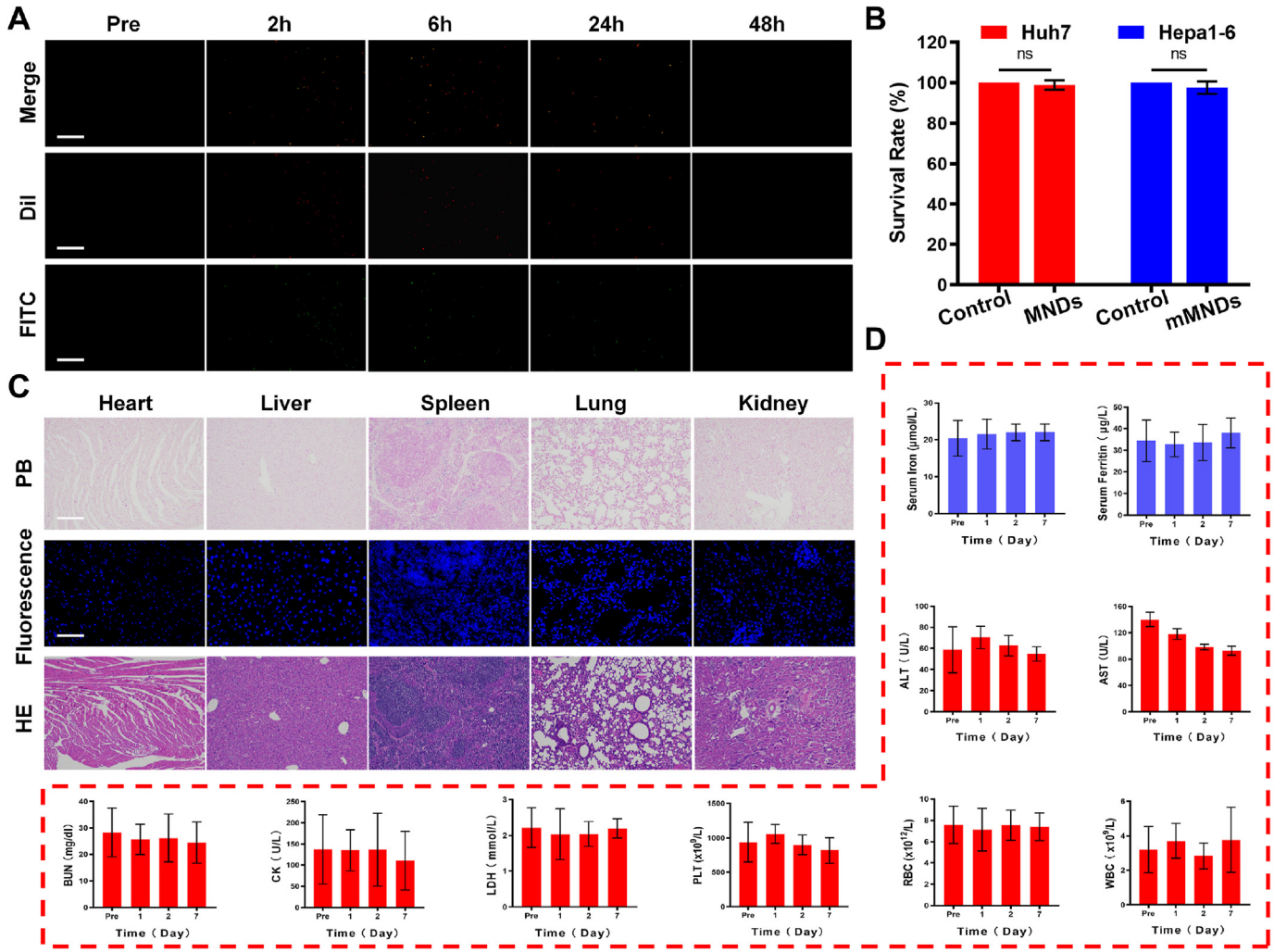

Fig. 2. Metabolism and biosafety of mMNDs. A Fluorescence microscopy **images of mMNDs in mice** urine. **The scale bar is 50 μm.** B **Cytotoxicity test** by a CCK-8 assay. **C Images** of autofluorescence, PB and HE staining 48 h following mMNDs injection. The scale bar of PB and HE staining is 50 μm, and the scale bar of fluorescence image is 100 μm. **D** Blood tests at different times.

urine was observed under fluorescence microscopy before, and 2 h, 6 h, 24 h, and 48 h after injecting mMNDs. A scattered dotted red-green light was observed at 2 h; it significantly increased at 6 h, decreased at 24 h, and diminished completely at 48 h (Fig. 2A). Thus, mMNDs can be excreted through the urine in 48 h.

The hearts, livers, spleens, lungs, and kidneys were stained with PB and HE staining 48 h following mMNDs injection. Only a small amount of PB staining was observed in the liver and spleen, and no evident autofluorescence was observed in the organ tissues (Fig. 2C). Thus, mMNDs were metabolized by the liver and spleen. No residues were found in the essential organs. HE staining of the organ tissues showed no significant abnormalities in the cellular morphology of the organ tissues.

The iron environment in mice was observed, routine blood and biochemical tests were obtained before and 1, 2, and 7 days after the injection of mMNDs. The results showed that all indicators were within normal levels during the follow-up period, both in the acute and relatively long term (Fig. 2D).

The results of above experiments indicate that mMNDs have good metabolism, biosafety, and reasonable clinical translation.

3.3. $Nd_2Fe_{14}B/Fe_3O_4$-PLGA performance testing

3.3.1. Phase transition and magnetic properties of $Nd_2Fe_{14}B/Fe_3O_4$-PLGA

Minimally invasive implantable bio-magnets are vital components of this project. The prepared bio-magnet precursor $Nd_2Fe_{14}B/Fe_3O_4$-PLGA has a dark gray liquid phase with good fluidity and can be inhaled into a 1 mL empty needle. The liquid-phase bio-magnetic precursor was injected smoothly into the cup with saline. The liquid-solid phase change occurred through solvent exchange to form a stable solid (Fig. 3A). As per macroscopic observation, the phase change time was 3 min. The ultrasonic detection of the *in vivo* phase change pattern of the bio-magnet precursor showed that the liquid-phase bio-magnet precursor was injected with a gray-black low-echo state; it gradually underwent solvent exchange and became solid after complete curing; it showed an echogenic solid-state (Fig. 3B). This indicates that the bio-magnet precursor can be fully cured *in vivo*. This feature firmly confines the implant within the tumor to avoid leakage and has a reliable safety profile. The cured bio-magnet precursor is magnetized further into a bio-magnet. The bio-magnet could attract Fe_3O_4; it shown specific magnetic susceptibility lines and magnetic poles. After demagnetization, the magnetism was significantly weakened; the bio-magnet no longer attracted Fe_3O_4 (Fig. 3C). The magnetic properties of the bio-magnet increased to 1.21 ± 0.11 mT after magnetization and weakened to 0.25 ± 0.07 mT after demagnetization (Fig. 3D), as measured by the Tesla magnetometer. Thus, the bio-magnet has good injectability and is a reliable precursor for minimally *in vivo* invasive implantation. This also demonstrates that the magnetic properties of the bio-magnet was adjustable as needed. The enhanced magnetic properties can effectively improve the primary

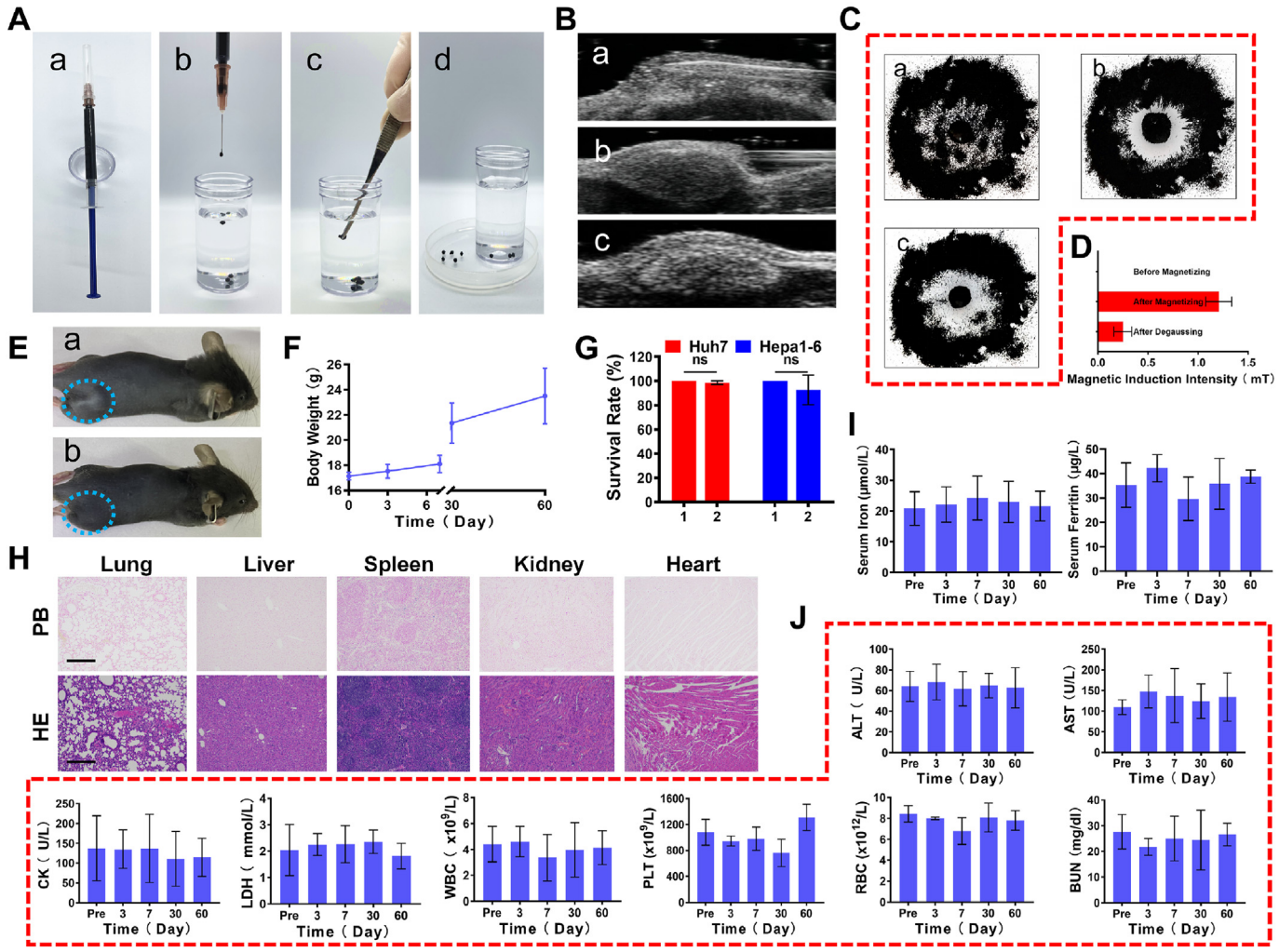

Fig. 3. Characterization and biosafety of $Nd_2Fe_{14}B/Fe_3O_4$-PLGA. **A** Photograph images of injectable $Nd_2Fe_{14}B/Fe_3O_4$-PLGA, before (a), in progress (b), after contacting with water (c), and eventually solid phase (d). **B** *In vivo* US imaging before (a) and after (b) the subcutaneous injection of $Nd_2Fe_{14}B/Fe_3O_4$-PLGA, and (c) eventually solid phase. **C** Photograph images of before magnetization (a), after magnetization (b), and after degaussing (c). **D** Magnetic properties of before magnetization, after magnetization and after degaussing. **E** Photograph images of $Nd_2Fe_{14}B/Fe_3O_4$-PLGA absorption *in vivo*, before (a) and after (b). **F** The body weight changes of mice. G **Cytotoxicity test** by a CCK-8 assay, 1 means control group, 2 means $Nd_2Fe_{14}B/Fe_3O_4$-PLGA group. **I** Blood tests of iron environment at different times. **H** Images of PB and HE staining after complete absorption of $Nd_2Fe_{14}B/Fe_3O_4$-PLGA. **The scale bar is 50 μm. J** Blood tests at different times.

targeting ability and increase the enrichment rate of MNDs/mMNDs in deep tumor tissues. The weakening of magnetic properties can cause MNDs/mMNDs to eliminate magnetic attraction and effectively implement secondary and tertiary targeting (autonomous selection of target cells and target receptors).

3.3.2. *Metabolism and biosafety of $Nd_2Fe_{14}B/Fe_3O_4$-PLGA*

The cytotoxicity of $Nd_2Fe_{14}B/Fe_3O_4$-PLGA was tested in Huh7 and Hepa1-6, respectively. The results showed that there was no significant difference in cell survival between the experimental group and the control group (Fig. 3G). Liquid-phase $Nd_2Fe_{14}B/Fe_3O_4$-PLGA was injected subcutaneously and observed in mice. After 2 months, there was complete absorption of $Nd_2Fe_{14}B/Fe_3O_4$-PLGA without skin breakdown (Fig. 3E), and the body weight increased steadily over time (Fig. 3F). The blood of mice was collected at the designated time-point for serum iron, serum ferritin, routine blood, and biochemical tests, and all indicators were within normal levels during the follow-up period (Fig. 3I and J). PB staining was performed on the organs obtained after complete absorption of $Nd_2Fe_{14}B/Fe_3O_4$-PLGA. Only a small amount of blue tissue was visible in the liver and spleen (Fig. 3H), which initially indicated that the liver and spleen could metabolize $Nd_2Fe_{14}B/Fe_3O_4$-PLGA. Concurrent HE staining was performed and minor histomorphological or pathological changes were observed (Fig. 3H). These results confirm that $Nd_2Fe_{14}B/Fe_3O_4$-PLGA had no adverse effects in mice, either in the acute or relatively long-term phase; thus, $Nd_2Fe_{14}B/Fe_3O_4$-PLGA can be metabolized easily and exhibited biosafety. They can be completely absorbed and metabolized after injection into the body without the need for presurgical removal, which is favorable for *in vivo* use. Considering the safety verification results of mMNDs, the clinical translation of mMNDs + bio-magnetic visualization and treatment systems is feasible.

3.4. *Performance of MNDs and mMNDs in vitro*

In the hierarchical targeting delivery strategy, each stage of targeting is critical to lay the necessary foundation for the final accurate drug delivery, just as a multi-stage rocket delivers a satellite to its target location, each stage provides the necessary power for the satellite to reach its final location (Fig. 4A).

3.4.1. *Selection of cell lines*

The high drug resistance and high proliferation ability of LCSCs are crucial for the low efficiency of HCC treatment; therefore, therapeutic

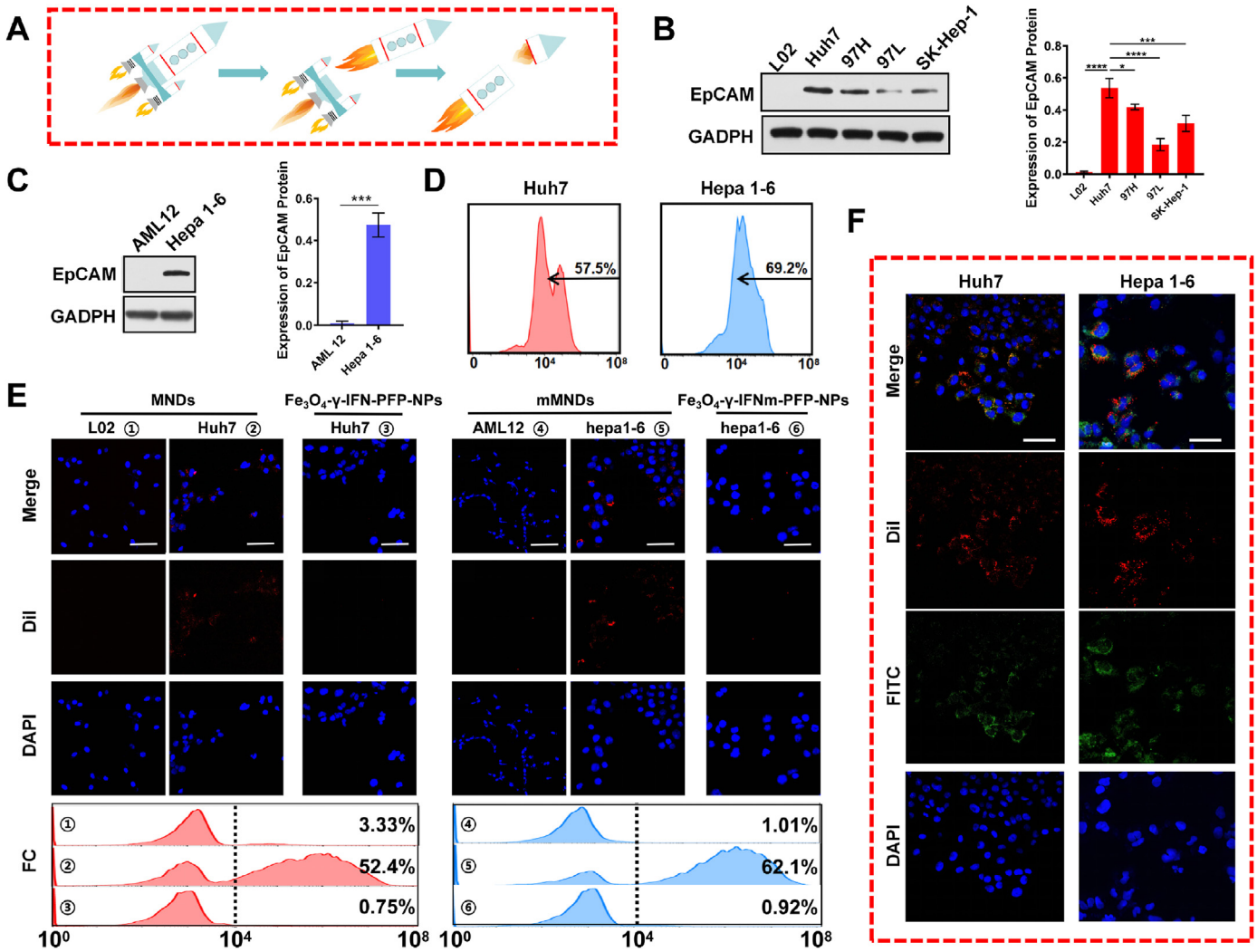

Fig. 4. Targeting Performance of MNDs and mMNDs *in vitro*. **A** Simulation of hierarchical target delivery strategy with rocket-delivered satellites. **B** WB analysis of EpCAM expression on human-derived cell lines. **C** WB analysis of EpCAM expression on murine-derived cell lines. **D** FC analyses of EpCAM expression rate on Huh7 cells and Hepa 1–6 cells. **E** CLSM images of human-derived or murine-derived cell lines treated by different nanoparticles, and FC analysis of secondary targeting ability. The scale bar is 50 μm. **F** CLSM images of Huh7 and Hepa 1–6 cells treated by MNDs or mMNDs shown secondary and tertiary targeting ability. The scale bar is 50 μm *p < 0.05, **p < 0.01, ***p < 0.001, ****p < 0.0001.

strategies targeting LCSCs can improve the cure rate of HCC [46,47]. EpCAM is considered a marker of LCSCs [47]; therefore, the MNDs and mMNDs prepared in this study used LCSCs with high expression of EpCAM as secondary targets. The expression of EpCAM in normal hepatocytes L02 and hepatoma cell lines Huh7, 97H, 97 L, and SK-Hep-1 was verified using WB, and the results showed that EpCAM was not expressed in normal hepatocytes L02; its expression was higher in the hepatoma cell line Huh7 than in other cell lines (Fig. 4B); therefore, Huh7 was selected as the experimental group for human-derived cells. WB was also used to verify the expression of EpCAM in murine-derived normal hepatocytes AML12 and murine-derived hepatocellular carcinoma cells Hepa1-6, and the results showed that EpCAM was not expressed in murine-derived normal hepatocytes AML12 and was highly expressed in murine hepatocellular carcinoma cells Hepa1-6 (Fig. 4C). After specifying the cell lines, the expression rate of EpCAM in various generic cell lines was determined using FC (Fig. 4D) to quantitatively evaluate the secondary targeting ability of MNDs and mMNDs at a later stage.

3.4.2. *Secondary targeting*

Secondary targeting enhances the enrichment of nanoparticles in target cells and provides the necessary conditions for precise drug delivery [48]. As observed in CLSM, after co-incubation with DiI-labeled MNDs and mMNDs with Huh7 and Hepa1-6 cells, respectively, red fluorescence was visible around the cytosolic membranes of most cells. Simultaneously, almost no red fluorescence was observed around L02 and AML12. No red fluorescence was observed around the cell membranes after co-incubation of nanoparticles without SNF peptides and EpCAM antibodies with Huh7 and Hepa1-6 (Fig. 4E). The quantitative FC analysis of the *in vitro* secondary targeting ability was almost consistent with the CLSM results (Fig. 4E). Thus, nanoparticles coupled with SNF peptides and EpCAM antibodies barely target normal liver cells but specifically target LCSCs, demonstrating the high precision of secondary targeting.

3.4.3. *Tertiary targeting*

As observed using CLSM, shells of MNDs/mMNDs loaded with FITC-labeled γ-IFN/γ-IFNm were labeled with DiI. After LIFU irradiation, the cells with red fluorescence around the cell membrane also had green fluorescence around them (Fig. 4F). The above results indicate that γ-IFN/γ-IFNm released by nanoparticle rupture can be efficiently targeted at the tertiary level based on the precise delivery of secondary

targeting.

The validation of secondary and tertiary targeting *in vitro* initially indicate that MNDs and mMNDs can deliver drugs accurately, enabling further validation of hierarchical targeting *in vivo*. The performance of *in vitro* primary targeting could not be discussed; thus, the study of primary targeting will be further elaborated in later *in vivo* experiments.

3.4.4. Treatment of MNDs in vitro

Gamma interferon can promote tumor cell apoptosis and increase the expressions of MHC proteins. It integrates chemotherapy and immunotherapy. MHC proteins are the basis of immunotherapy in this study. The low expression of MHC proteins can help tumor cells escape the recognition and killing of immune cells, and MHC proteins are usually in a low expression in tumor cells [49,50]. By increasing the expression of MHC proteins in tumor cells, it helps to improve antigen presentation and enhance the anti-tumor T cell response [49]. MHC proteins are different in human and mice, HLA-I proteins in Human, while H-2 proteins in mice. Because the experiment involved human and mouse HCC models, we verified these two proteins according to the experimental species.

WB results showed that compared to the control group, an increase in HLA-I was observed in the MNDs, Fe_3O_4-γ–IFN–PFP-NPs, Fe_3O_4-γ–IFN–PFP-NPs + LIFU and MNDs + LIFU groups (Fig. 5A and E). The increase in HLA-I was the most apparent in the MNDs + LIFU group, which confirmed the secondary targeted delivery. The binding rate of γ-IFN to receptors on the cell membrane surface was higher, and drug efficacy was most apparent. The results of the quantitative FC assay were consistent with the WB results, i.e., the HLA-I expression rate of the MNDs + LIFU group reached 20.20%, which was 5.3 times higher than that of the control group at 3.81% (Fig. 5C and F). Calcein-AM/PI cell double staining was used to verify the effect of different treatment groups on the survival of Huh7 cells. In the CLSM images, living cells were stained green by calcein-AM and dead cells were stained red by PI. The results showed that almost all Huh7 cells in the control, MNDs, Fe_3O_4-γ–IFN–PFP-NPs, and Fe_3O_4-PFP-NPs:SNF groups were green-stained live cells; red-stained dead cells were occasionally observed. However, cells in the remaining groups were red-stained died cells to varying degrees. The Fe_3O_4-γ–IFN–PFP-NPs + LIFU and MNDs + LIFU groups were significantly red-stained, the MNDs + LIFU group showed maximum number of red-stained cells (Fig. 5B). The results of quantitative FC for apoptosis were consistent with the above results (Fig. 5D and G). Thus, physical killing by LIFU irradiation and chemical killing by drugs produce different degrees of damage to Huh7 cells. MNDs exert a more significant therapeutic effect through secondary and tertiary targeting of LCSCs, especially in combination with physical and chemical injury.

In conclusion, MNDs and mMNDs perform well with secondary and tertiary targeting *in vitro*. The precise delivery of secondary targeting helps in tertiary targeting and optimizes the therapeutic effect of drugs. Further, *in vitro* treatment results showed that MNDs performed well in the direct killing of tumor cells (physiotherapy and chemotherapy) and enhancing antigen presentation (immunotherapy), laying the foundation for further *in vivo* treatment. The therapeutic effects of mMNDs are not discussed here, and the relevant part will be further elaborated in *in vivo* experiments.

3.5. Visualization and accurate targeting of mMNDs + Bio-magnet in vivo

3.5.1. Fluorescence reveals bio-magnet-mediated primary targeting

A large number of mMNDs in blood vessels are guided into the tumor

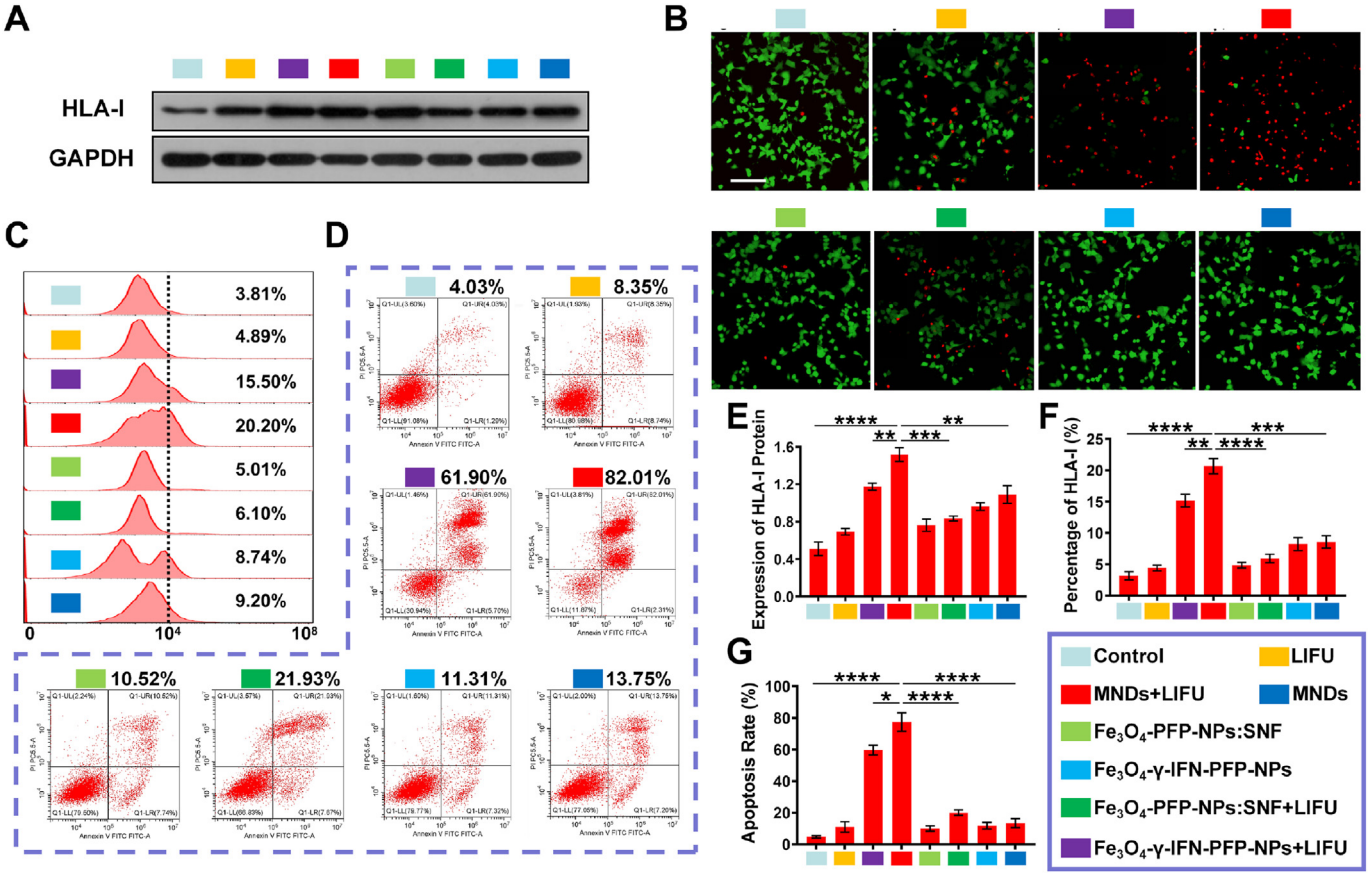

Fig. 5. Treatment of MNDs *in vitro*. **A&E** WB analysis of HLA-I expression on Huh7 cells treated by different nanoparticles. **C&F** FC analysis of HLA-I expression on Huh7 cells treated by different nanoparticles. **B** The Calcian-AM/PI staining of Huh7 cells after different treatments. The green fluorescence shows living cells and the red fluorescence represents dead cells. The scale bar is 50 μm. **D&G** FC analysis of apoptosis after different treatments. *p < 0.05, **p < 0.01, ***p < 0.001, ****p < 0.0001.

and its deeper parts by an intra-tumoral magnetic field, which is the first efficient stage of graded targeting. In small-animal *in vivo* fluorescence imaging, the mMNDs + Bio-magnet group exhibited a significant fluorescence signal 3 h after mMNDs injection compared with the mMNDs group, with a mean fluorescence intensity of (16.79 ± 1.04) × 10^6 nW, which was 11.99 times higher than that of the mMNDs group (1.40 ± 0.33) × 10^6 nW. The mMNDs group showed a significant fluorescence signal of (7.49 ± 1.33) × 10^6 nW at 12 h, and the fluorescence intensity of the mMNDs + Bio-magnet group at 3 h was 2.24 times higher than that of the mMNDs group. The bio-magnet demagnetization treatment performed at 3 h, and a significant fluorescence signal remained at 12 and 24 h (Fig. 6A and C). The mean fluorescence intensity of tumors in the

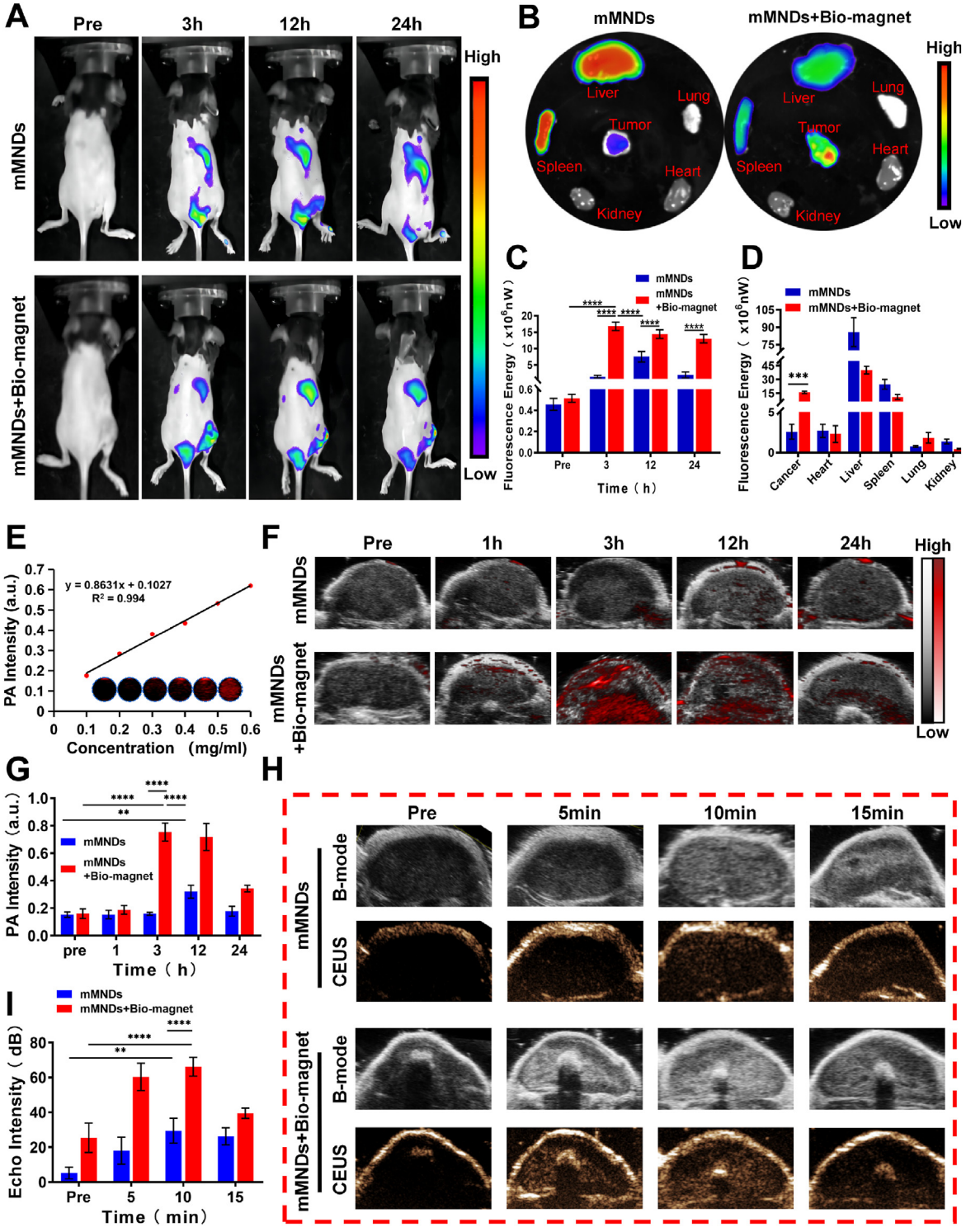

Fig. 6. Visualization and accurate targeting of mMNDs + Bio-magnet *in vivo*. **A** *In vivo* imaging of mMNDs in C57 tumor-bearing mice. **B** *Ex vivo* fluorescence imaging of main organs and tumors in different groups. **C** The statistical fluorescence intensity of tumors in different groups at different time. **D** The statistical fluorescence intensity of main organs and tumors in different groups after 24 h. **E** PA imaging and intensity of the mMNDs. **F** PA imaging of mMNDs in C57 tumor-bearing mice. **G** The statistical PA intensity of tumors in different groups at different time. **H** US imaging of mMNDs in C57 tumor-bearing mice. **I** The statistical CEUS echo intensity of tumors in different groups at different time. *p < 0.05, **p < 0.01, ***p < 0.001, ****p < 0.0001.

mMNDs + Bio-magnet group was also significantly stronger than that in the mMNDs group (Fig. 6B and D) when the tumors and organs were removed after 24 h, and fluorescence intensity was measured using IndiGo software. The above results indicate that bio-magnet-mediated primary targeting has superior targeting ability; it can significantly increase the drug enrichment rate in target tissues. Meanwhile, the fluorescence intensity of the liver and spleen was the most obvious among all organs in both groups (Fig. 6B and D), which also indicated that the mMNDs were metabolized through the liver and spleen.

3.5.2. Photoacoustic (PA) imaging showing bio-magnet-mediated primary targeting

mMNDs have enhanced PA visualization properties owing to their iron content, which allows the visualization and supervision of primary targeting. The small-animal PA imager showed that the visualization ability of mMNDs was positively correlated with their concentration (Fig. 6E). In mice, the mMNDs + Bio-magnet group exhibited a significant PA signal 3 h after mMNDs injection compared to the pre-injection period. Simultaneously, the bio-magnet demagnetization treatment was administered and a significant PA signal was observed at 12 h, which was attenuated in 24 h because of the *in vivo* self-clearing effect (Fig. 6F). Quantitative analysis of the PA signal intensity of the two groups showed that the PA intensity of the mMNDs + Bio-magnet group at 3 h was 4.74 times higher than that of the mMNDs group; it was 2.36 times higher than that of the mMNDs group at 12 h (Fig. 6G). These findings were consistent with those of small-animal *in vivo* fluorescence, indicating that primary targeting mediated by bio-magnet mediation can significantly improve the enrichment rate of mMNDs in tumors, initiating precise diagnosis and treatment. Additionally, PA imaging can be used to monitor primary targeting. Primary targeting can enhance PA imaging and help in the diagnosis and treatment of mutually optimized tumors.

3.5.3. US imaging shows LIFU irradiation-controlled drug release

The mMND-loaded PFP can undergo liquid-gas phase change under LIFU irradiation, which enhances US imaging. According to the results of *in vivo* fluorescence and PA imaging, the mMNDs group was subjected LIFU 3 W/cm^2 irradiation for 5, 10, and 15 min after 12 h of mMNDs injection and 3 h of mMNDs injection in the mMNDs + Bio-magnet group, and the results were detected using ultrasonic detection, which showed that both groups were visible after 5 min, but the mMNDs + Bio-magnet group was more significant (Fig. 6I). After 10 min, both groups showed a substantial shadowing effect, but the mMNDs + Bio-magnet group showed the most significant shadowing. After 15 min, both groups still showed shadowing. However, the shadowing effect was weaker than before owing to rupture of most of the liquid-gas phase change of the nanoparticles (Fig. 6H). Quantitative analysis of grayscale values (Fig. 6I) showed that both the mMNDs and mMNDs + Bio-magnet groups showed differences at 10 min compared to the pre, indicating that LIFU irradiation could better stimulate the liquid-gas phase change of mMND-loaded PFP and thus, release the drug; this is consistent with *in vitro* phase change and drug release results (Fig. 1G and L). The ability of mMNDs to undergo liquid-gas phase changes under LIFU irradiation can enhance ultrasound imaging and release drugs at regular intervals, which also enables precise diagnosis and treatment. The mean grayscale values of the mMNDs + Bio-magnet group were higher than those of the mMNDs group, demonstrating that primary targeting could significantly increase the enrichment rate of mMNDs in tumor tissues.

3.5.4. Observation of autofluorescence in tumor tissue sections

Tumor tissue sections were obtained from mMNDs and mMNDs + Bio-magnet groups and observed under CLSM for autofluorescence. Deep tumor tissue was used for the mMNDs group, and the tissue near the Bio-magnet was used for the mMNDs + Bio-magnet group. The shells of injected mMNDs were stained with DiI, and mMNDs were loaded with fluorescein isothiocyanate (FITC)-labeled γ-IFNm. A small amount of red-green fluorescence was observed in the mMNDs group, whereas the mMNDs + Bio-magnet group showed abundant red-green fluorescence with a centripetal enrichment trend centered around the bio-magnet (Fig. 7). The above results reconfirm that the mMNDs + Bio-magnet system can enhance the primary targeting ability and increase the number of nanoparticles that can enter deep into the tumor. Nanoparticles can be more efficient for secondary targeting after demagnetization, and LIFU irradiation can release the drug and carry out tertiary targeting.

In summary, the use of primary targeting to enhance the enrichment of mMNDs at tumor sites is well demonstrated using *in vivo* fluorescence and photoacoustic imaging in the system. And compared with the traditional in situ injection treatment strategy, this system can visual monitoring of the disease treatment process. Visualized dual-modality imaging combining PA and US can effectively present the graded targeting situation; it also confirm the superior precision targeting ability of the mMNDs + Bio-magnet system from a macroscopic visualization perspective. Simultaneously, the tissue sections further demonstrate the feasibility and efficiency of graded targeting at the microscopic level. Thus, precise targeting and visualization supervision complement each other.

3.6. In vivo treatment of mMNDs + Bio-magnet system

A previous *in vitro* study confirmed that our designed treatment strategy could effectively promote apoptosis of tumor cell and expression of MHC proteins; to further confirm our idea, we conducted *in vivo* treatment experiments on bilaterally tumor-bearing C57 mice. The treatment effect was evaluated by monitoring the growth of the primary and distant tumors, and the results showed that the most significant reduction of bilateral tumors was observed in the mMNDs + Bio-magnet + LIFU group compared with the control, mMNDs + LIFU and Fe_3O_4-γ-IFNm-PFP-NPs + Bio-magnet + LIFU groups (Fig. 8A and E). It demonstrated that the tumors on the left side of the mMNDs + Bio-magnet + LIFU group received more increased drug enrichment and accurate physical, chemical, and immunological treatments by hierarchical targeting. The tumors on the right side, which did not receive immediate treatment, were also suppressed, mainly due to the antitumor immune response generated by the treatment of the left tumor, which directly confirms that this system can produce practical immunotherapeutic effects.

To further compare the treatment effects, the left tumors of each group were collected for immunofluorescence staining and TUNEL staining. The tumor tissue H-2 expression rate and apoptosis were quantified using FC. As shown in Fig. 8C, green fluorescence represents H-2 expression. Compared with the control group, increased H-2 was observed in the mMNDs + LIFU, Fe_3O_4-γ-IFNm-PFP-NPs + Bio-magnet + LIFU, and mMNDs + Bio-magnet + LIFU groups, with the most significant increase in the mMNDs + Bio-magnet + LIFU group. In contrast, the increase in H-2 was not significant in the saline + LIFU, mMNDs, mMNDs + Bio-magnet, and Fe_3O_4-PFP-NPs:EpC + Bio-magnet + LIFU groups (Fig. 8C). In quantitative analysis using FC, the H-2 expression in the mMNDs + Bio-magnet + LIFU group was 7.11-fold, 2.08-fold, and 1.32-fold higher than that in the control, mMNDs + LIFU, and Fe_3O_4-γ-IFNm-PFP-NPs + Bio-magnet + LIFU groups, respectively (Fig. 8F and H). Thus, using precise delivery of graded targeting combined with LIFU irradiation, the anti-tumor effect of mMNDs can be significantly enhanced. TUNEL staining showed that LIFU irradiation, chemotherapy, and immunotherapy under graded targeting conditions resulted in significant green fluorescence in the mMNDs + Bio-magnet + LIFU group, suggesting significantly greater tumor cell apoptosis in this group than in the remaining groups (Fig. 8B). The results of apoptosis detection using FC were consistent with the results of TUNEL staining, and the apoptosis rate in the mMNDs + Bio-magnet + LIFU group was as high as 74.78% (Fig. 8G and I).

Meanwhile, there was no significant weight loss in the mMNDs + Bio-magnet + LIFU group compared to the control group (Fig. 8D), and no

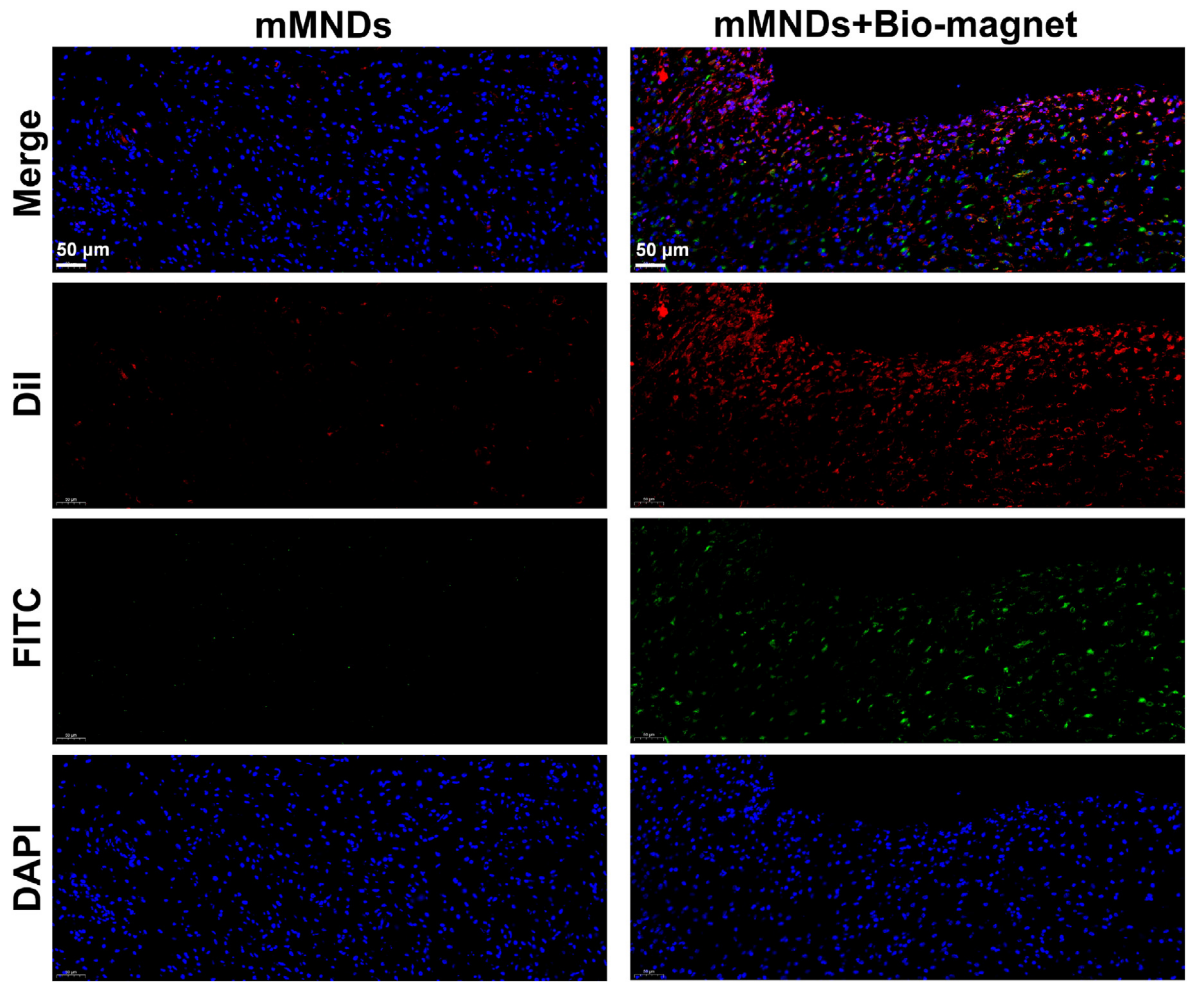

Fig. 7. CLSM images of autofluorescence in tumor tissue sections. The blue fluorescence shows nucleus, the red fluorescence is Dil-labeled EpCAM antibodies, and the red fluorescence is FITC-labeled γ-IFNm.

mouse mortality was observed throughout the treatment process. This observation, combined with the above experimental results, confirms the effectiveness of the system.

As a traditional cancer treatment modality, chemotherapy alone can inhibit tumor growth to a certain extent [51]. However, most chemotherapeutic agents have suboptimal accumulation barriers [52]; these severely impede clinical treatment when combined with tumor resistance [5,51]. We designed a graded targeting multifunctional system that significantly improved drug enrichment in tumor tissues through primary targeting, solving the above-mentioned limitations effectively. Targeted LCSCs combined with the trinity treatment strategy can effectively address the adverse consequences of high drug resistance in HCC through physical, chemical, and immune killing, and optimize anti-tumor therapy. Moreover, the feasibility of this system was demonstrated in different species (human and murine) of HCC models. Studies on using reactive oxygen species (ROS) to treat tumors have emerged in recent years [53,54]. Most of them have discussed that Fe_3O_4 is the main component because the Fenton reaction involving Fe_3O_4 can produce ROS [55,56], and mitochondria are also the natural oxygen production plant in the body [54]. The combination of Fe_3O_4 and mitochondrial targeting is a feasible direction. ROS can also damage normal cells. For example, the activation of the renin angiotensin aldosterone system can increase ROS, which can lead to liver fibrosis and then lead to liver cancer [57]. The ability to accurately regulate Fe_3O_4 by using a magnetic field is also expected to regulate the aldosterone system accurately, so that it can change its role in the lesion site. It is also a direction to explore the combined use of nanoantioxidants when necessary to avoid the adverse reactions of the aldosterone system [58]. Moreover, the shell platform constructed by Fe_3O_4 combined with liposomes in this system has a strong assembly ability, and its application in other diseases can be explored in the future.

Thus, this system is expected to improve the precision of targeted drugs and the drug enrichment rate through graded precision targeting; it can provide a new strategy for more accurate visual diagnosis and treatment of tumor.

4. Conclusion

The proposed visualization and treatment system based on hierarchical precision targeting is practical and feasible. The multifunctional magnetic nanoparticles loaded with Fe_3O_4 were precisely targeted to HCC tissue-LCSCs- Gamma interferon receptors at three levels, mediated by an *in vivo* bio-magnet, SNF peptide/EpCAM antibody, and γ-IFN/γ-IFNm hierarchy. Compared to other targeting strategies, in the primary targeting strategy, the magnetically responsive targeted delivery system can provide a solid force to attract magnetic nanoparticles to the tumor region, which counteracts the high interstitial pressure inside the tumor and increases targeted enrichment of nanoparticles. The high accumulation of nanoparticles at the tumor site could enhance photoacoustic and ultrasound molecular imaging for further diagnosis. After degaussing, the SNF peptide/EpCAM antibody mediates secondary targeting, and nanoparticles actively target LCSCs and deliver drugs around them. Under LIFU irradiation, the nanoparticle phase changes blast to kill some tumor cells, and the released γ-IFN/γ-IFNm are more enriched in LCSCs to

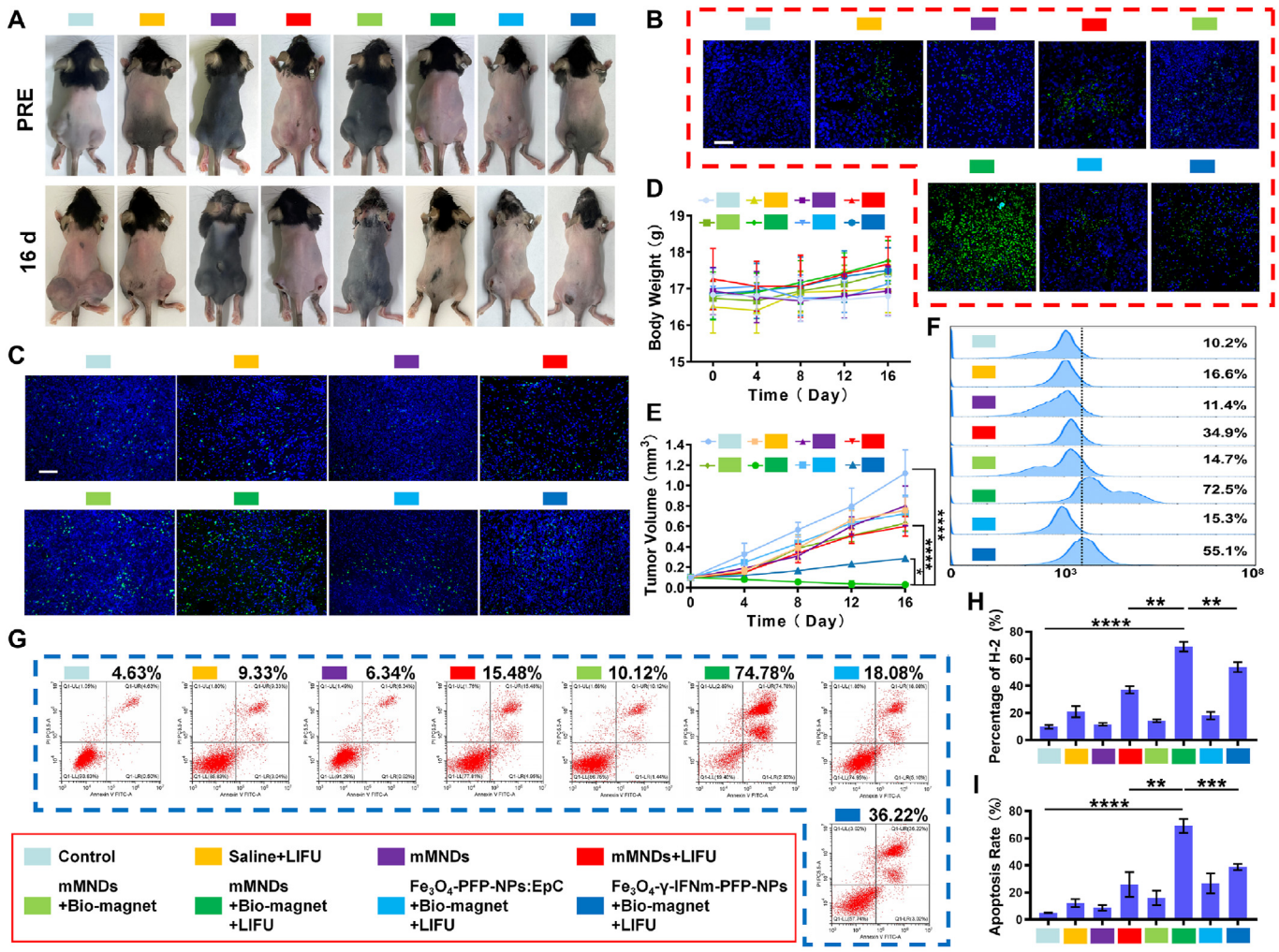

Fig. 8. *In vivo* treatment of mMNDs + Bio-magnet system. **A** Pictures of mice in different groups. **B** TUNEL staining in different tumor tissue sections, and FC analysis of tumor tissue apoptosis in different tumor tissues. The scale bar is 50 μm. **C&H** Immunofluorescence staining of H-2 (green) in different tumor tissue sections. The scale bar is 50 μm. **D** Time-body-weight curves of tumor-bearing mice in the different treatment groups. **E** Time-tumor-volume curves of the left tumor in the different treatment groups. **F** FC analysis of H-2 expression rate in different tumor tissues. **G&I** FC analysis of Tumor cells apoptosis. *p < 0.05, **p < 0.01, ***p < 0.001, ****p < 0.0001.

finally achieve tertiary targeting. After binding to the receptor, γ-IFN/γ-IFNm can effectively promote tumor cell apoptosis, up-regulate MHC proteins expression, and finally "kill" the tumor in the crib through physical injury, chemotherapy, and immunotherapy. This series of measures is a powerful approach for making the treatment of HCC more efficient and thorough. Moreover, the feasibility of this system has been demonstrated in different species (human and murine) of HCC models. In conclusion, a visual diagnosis and treatment system based on hierarchical precision targeting has a promising potential.

Credit author statement

Shasha Shi: Conceptualization, Methodology, Formal analysis, Investigation, Writing-original draft, Visualization, Validation. **Huipu Li**: Conceptualization, Formal analysis, Investigation. **Xi Zheng**: Methodology, Validation. **Lin Lv**: Methodology, Validation. **Shengtao Liao**: Formal analysis, Writing – review. **Peng Lu**: Methodology, Investigation, Writing – review. **Maoxia Liu**: Methodology, Validation. **Hongyun Zhao**: Resources, Writing-review & editing, Supervision, Project administration, Funding acquisition. **Zhechuan Mei**: Resources, Writing-review & editing, Supervision, Project administration, Funding acquisition.

Declaration of competing interest

The authors declare that they have no known competing financial interests or personal relationships that could have appeared to influence the work reported in this paper.

Acknowledgements

This work was financially supported by National Natural Science Foundation of China (No. 82173360); National Natural Science Foundation Youth Project (No. 81801714); Senior Medical Talents Program of Chongqing for Yong and Middle-aged (No. 11-020); Kuanren Talents Program of the second affiliated hospital of Chongqing Medical University (No. 2021240308, 13-003-023).

References

[1] H. Yang, Y.H. Kuo, Z.I. Smith, J. Spangler, Targeting cancer metastasis with antibody therapeutics, WIREs Nanomedicine Nanobiotechnology 13 (2021) e1698.
[2] E. Blass, P.A. Ott, Advances in the development of personalized neoantigen-based therapeutic cancer vaccines, Nat. Rev. Clin. Oncol. 18 (2021) 215–229.
[3] A.G. Waks, E.P. Winer, Breast cancer treatment: a review, JAMA 321 (2019) 288–300.
[4] D. Rosenblum, N. Joshi, W. Tao, J.M. Karp, D. Peer, Progress and challenges towards targeted delivery of cancer therapeutics, Nat. Commun. 9 (2018) 1410.

[5] T. Saha, K.E. Lukong, Breast cancer stem-like cells in drug resistance: a review of mechanisms and novel therapeutic strategies to overcome drug resistance, Front. Oncol. 12 (2022), 856974.

[6] S. Xia, Y. Pan, Y. Liang, J. Xu, X. Cai, The microenvironmental and metabolic aspects of sorafenib resistance in hepatocellular carcinoma, EBioMedicine 51 (2020), 102610.

[7] M.J. Mitchell, M.M. Billingsley, R.M. Haley, M.E. Wechsler, N.A. Peppas, R. Langer, Engineering precision nanoparticles for drug delivery, Nat. Rev. Drug Discov. 20 (2021) 101–124.

[8] N. Amreddy, A. Babu, R. Muralidharan, J. Panneerselvam, A. Srivastava, R. Ahmed, M. Mehta, A. Munshi, R. Ramesh, Recent advances in nanoparticle-based cancer drug and gene delivery, Adv. Cancer Res. 137 (2018) 115–170.

[9] T.L. Rapp, C.A. DeForest, Targeting drug delivery with light: a highly focused approach, Adv. Drug Deliv. Rev. 171 (2021) 94–107.

[10] A. Eftekhari, M. Hasanzadeh, S. Sharifi, S.M. Dizaj, R. Khalilov, E. Ahmadian, Bioassay of saliva proteins: the best alternative for conventional methods in non-invasive diagnosis of cancer, Int. J. Biol. Macromol. 124 (2019) 1246–1255.

[11] L.P. Datta, S. Manchineella, T. Govindaraju, Biomolecules-derived biomaterials, Biomaterials 230 (2020), 119633.

[12] R.K. Jain, T. Stylianopoulos, Delivering nanomedicine to solid tumors, Nat. Rev. Clin. Oncol. 7 (2010) 653–664.

[13] Y. Zhang, J. Cao, Z. Yuan, Strategies and challenges to improve the performance of tumor-associated active targeting, J. Mater. Chem. B. 8 (2020) 3959–3971.

[14] W. Zhang, A. Mehta, Z. Tong, L. Esser, N.H. Voelcker, Development of polymeric nanoparticles for blood-brain barrier transfer-strategies and challenges, Adv. Sci. Weinh. Baden-Wurtt. Ger. 8 (2021), 2003937.

[15] Q. Li, E. Hu, K. Yu, M. Lu, R. Xie, F. Lu, B. Lu, R. Bao, G. Lan, Magnetic field-mediated Janus particles with sustained driving capability for severe bleeding control in perforating and inflected wounds, Bioact. Mater. 6 (2021) 4625–4639.

[16] F. Zhang, G. Lu, X. Wen, F. Li, X. Ji, Q. Li, M. Wu, Q. Cheng, Y. Yu, J. Tang, L. Mei, Magnetic nanoparticles coated with polyphenols for spatio-temporally controlled cancer photothermal/immunotherapy, J. Control. Release Off. J. Control. Release Soc. 326 (2020) 131–139.

[17] T. Cristofolini, M. Dalmina, J.A. Sierra, A.H. Silva, A.A. Pasa, F. Pittella, T.B. Creczynski-Pasa, Multifunctional hybrid nanoparticles as magnetic delivery systems for siRNA targeting the HER2 gene in breast cancer cells, Mater, Sci. Eng. C Mater. Biol. Appl. 109 (2020), 110555.

[18] H.W. Cheng, H.Y. Tsao, C.S. Chiang, S.Y. Chen, Advances in magnetic nanoparticle-mediated cancer immune-theranostics, Adv. Healthc. Mater. 10 (2021), e2001451.

[19] B. Shapiro, S. Kulkarni, A. Nacev, S. Muro, P.Y. Stepanov, I.N. Weinberg, Open challenges in magnetic drug targeting, Wiley Interdiscip. Rev. Nanomed. Nanobiotechnol. 7 (2015) 446–457.

[20] Y. Chen, L. Jiang, R. Wang, M. Lu, Q. Zhang, Y. Zhou, Z. Wang, G. Lu, P. Liang, H. Ran, H. Chen, Y. Zheng, Injectable smart phase-transformation implants for highly efficient *in vivo* magnetic-hyperthermia regression of tumors, Adv. Mater. Deerfield Beach Fla. 26 (2014) 7468–7473.

[21] R. Fratila, A. Benabou, A. Tounzi, J.C. Mipo, Nonlinear modeling of magnetization loss in permanent magnets, IEEE Trans. Magn. 48 (2012) 2957–2960.

[22] J. Wang, W. Song, X. Wang, Z. Xie, W. Zhang, W. Jiang, S. Liu, J. Hou, Y. Zhong, J. Xu, H. Ran, D. Guo, Tumor-self-targeted "thermoferroptosis-sensitization" magnetic nanodroplets for multimodal imaging-guided tumor-specific therapy, Biomaterials 277 (2021), 121100.

[23] Z. Wang, G. Wang, T. Kang, S. Liu, L. Wang, H. Zou, Y. Chong, Y. Liu, $BiVO_4$/Fe_3O_4@polydopamine superparticles for tumor multimodal imaging and synergistic therapy, J. Nanobiotechnol. 19 (2021) 90.

[24] H. Huang, G. Yuan, Y. Xu, Y. Gao, Q. Mao, Y. Zhang, L. Bai, W. Li, A. Wu, W. Hu, Y. Pan, G. Zhou, Photoacoustic and magnetic resonance imaging-based gene and photothermal therapy using mesoporous nanoagents, Bioact. Mater. 9 (2022) 157–167.

[25] L. Walcher, A.K. Kistenmacher, H. Suo, R. Kitte, S. Dluczek, A. Strauß, A.-R. Blaudszun, T. Yevsa, S. Fricke, U. Kossatz-Boehlert, Cancer stem cells-origins and biomarkers: perspectives for targeted personalized therapies, Front. Immunol. 11 (2020) 1280.

[26] J.A. Clara, C. Monge, Y. Yang, N. Takebe, Targeting signalling pathways and the immune microenvironment of cancer stem cells - a clinical update, Nat. Rev. Clin. Oncol. 17 (2020) 204–232.

[27] N.K. Lytle, A.G. Barber, T. Reya, Stem cell fate in cancer growth, progression and therapy resistance, Nat. Rev. Cancer 18 (2018) 669–680.

[28] H.Y. Wang, B. Zhang, J.N. Zhou, D.X. Wang, Y.C. Xu, Q. Zeng, Y.L. Jia, J.F. Xi, X. Nan, L.J. He, W. Yue, X.T. Pei, Arsenic trioxide inhibits liver cancer stem cells and metastasis by targeting SRF/MCM7 complex, Cell Death Dis. 10 (2019) 453.

[29] G. Castelli, E. Pelosi, U. Testa, Liver cancer: molecular characterization, clonal evolution and cancer stem cells, Cancers 9 (2017) E127.

[30] A. Takaoka, Y. Mitani, H. Suemori, M. Sato, T. Yokochi, S. Noguchi, N. Tanaka, T. Taniguchi, Cross talk between interferon-gamma and -alpha/beta signaling components in caveolar membrane domains, Science 288 (2000) 2357–2360.

[31] T. Sakatani, Y. Kita, M. Fujimoto, T. Sano, A. Hamada, K. Nakamura, H. Takada, T. Goto, A. Sawada, S. Akamatsu, T. Kobayashi, IFN-gamma expression in the tumor microenvironment and CD8-positive tumor-infiltrating lymphocytes as prognostic markers in urothelial cancer patients receiving pembrolizumab, Cancers 14 (2022) 263.

[32] C. Nakajima, Y. Uekusa, M. Iwasaki, N. Yamaguchi, T. Mukai, P. Gao, M. Tomura, S. Ono, T. Tsujimura, H. Fujiwara, T. Hamaoka, A role of interferon-gamma (IFN-gamma) in tumor immunity: T cells with the capacity to reject tumor cells are generated but fail to migrate to tumor sites in IFN-gamma-deficient mice, Cancer Res. 61 (2001) 3399–3405.

[33] D.R. Johnson, J.S. Pober, Tumor necrosis factor and immune interferon synergistically increase transcription of HLA class I heavy- and light-chain genes in vascular endothelium, Proc. Natl. Acad. Sci. U.S.A. 87 (1990) 5183–5187.

[34] K.M. Detjen, K. Farwig, M. Welzel, B. Wiedenmann, S. Rosewicz, Interferon gamma inhibits growth of human pancreatic carcinoma cells via caspase-1 dependent induction of apoptosis, Gut 49 (2001) 251–262.

[35] F. Li, Q. Li, J. Wang, C. Zhan, C. Xie, W. Lu, Effects of interferon-gamma liposomes targeted to platelet-derived growth factor receptor-beta on hepatic fibrosis in rats, J. Control. Release Off. J. Control. Release Soc. 159 (2012) 261–270.

[36] B. Yang, J. Shi, Developing new cancer nanomedicines by repurposing old drugs, Angew. Chem., Int. Ed. Engl. 59 (2020) 21829–21838.

[37] X. Ma, X. Kang, L. He, J. Zhou, J. Zhou, M.B. Sturm, D.G. Beer, R. Kuick, D.J. Nancarrow, H.D. Appelman, Z. Pang, W. Li, C. Zhang, W. Zhang, Y. Zhang, T.D. Wang, M. Li, Identification of tumor specific peptide as EpCAM ligand and its potential diagnostic and therapeutic clinical application, Mol. Pharm. 16 (2019) 2199–2213.

[38] H. Li, S. Shi, M. Wu, W. Shen, J. Ren, Z. Mei, H. Ran, Z. Wang, Y. Tian, J. Gao, H. Zhao, iRGD peptide-mediated liposomal nanoparticles with photoacoustic/ultrasound dual-modality imaging for precision theranostics against hepatocellular carcinoma, Int. J. Nanomed. 16 (2021) 6455–6475.

[39] B. Liang, K. Yu, Y. Ling, M. Kolios, A. Exner, Z. Wang, B. Hu, G. Zuo, Y. Chen, Y. Zheng, An artificially engineered "tumor bio-magnet" for collecting blood-circulating nanoparticles and magnetic hyperthermia, Biomater. Sci. 7 (2019) 1815–1824.

[40] J. Hou, J. Zhou, M. Chang, G. Bao, J. Xu, M. Ye, Y. Zhong, S. Liu, J. Wang, W. Zhang, H. Ran, Z. Wang, Y. Chen, D. Guo, LIFU-responsive nanomedicine enables acoustic droplet vaporization-induced apoptosis of macrophages for stabilizing vulnerable atherosclerotic plaques, Bioact. Mater. 16 (2022) 120–133.

[41] L. Fotouhi, M.M. Heravi, V. Zadsirjan, P.A. Atoi, Electrochemically induced Michael addition reaction: an overview, Chem. Rec. N. Y. N. 18 (2018) 1633–1657.

[42] R. Roskoski, Orally effective FDA-approved protein kinase targeted covalent inhibitors (TCIs), Pharmacol. Res. 165 (2021), 105422.

[43] A. Yang, B. Qiao, E.M. Strohm, J. Cao, Z. Wang, X. Yuan, Y. Luo, Y. Sun, Thrombin-responsive engineered nanoexcavator with full-thickness infiltration capability for pharmaceutical-free deep venous thrombosis theranostics, Biomater. Sci. 8 (2020) 4545–4558.

[44] X. H, C. Y, Energy-converting nanomedicine, Small Weinh. Bergstr. Ger. 15 (2019).

[45] N.D. Donahue, H. Acar, S. Wilhelm, Concepts of nanoparticle cellular uptake, intracellular trafficking, and kinetics in nanomedicine, Adv. Drug Deliv. Rev. 143 (2019) 68–96.

[46] K. Nio, T. Yamashita, S. Kaneko, The evolving concept of liver cancer stem cells, Mol. Cancer 16 (2017) 4.

[47] T.K.W. Lee, X.Y. Guan, S. Ma, Cancer stem cells in hepatocellular carcinoma - from origin to clinical implications, Nat. Rev. Gastroenterol. Hepatol. 19 (2022) 26–44.

[48] H. Zhao, M. Wu, L. Zhu, Y. Tian, M. Wu, Y. Li, L. Deng, W. Jiang, W. Shen, Z. Wang, Z. Mei, P. Li, H. Ran, Z. Zhou, J. Ren, Cell-penetrating peptide-modified targeted drug-loaded phase-transformation lipid nanoparticles combined with low-intensity focused ultrasound for precision theranostics against hepatocellular carcinoma, Theranostics 8 (2018) 1892–1910.

[49] K. Yamamoto, A. Venida, J. Yano, D.E. Biancur, M. Kakiuchi, S. Gupta, A.S.W. Sohn, S. Mukhopadhyay, E.Y. Lin, S.J. Parker, R.S. Banh, J.A. Paulo, K.W. Wen, J. Debnath, G.E. Kim, J.D. Mancias, D.T. Fearon, R.M. Perera, A.C. Kimmelman, Autophagy promotes immune evasion of pancreatic cancer by degrading MHC-I, Nature 581 (2020) 100–105.

[50] M.L. Axelrod, R.S. Cook, D.B. Johnson, J.M. Balko, Biological consequences of MHC-II expression by tumor cells in cancer, Clin. Cancer Res. Off. J. Am. Assoc. Cancer Res. 25 (2019) 2392–2402.

[51] T. Das, U. Anand, S.K. Pandey, C.R. Ashby, Y.G. Assaraf, Z.-S. Chen, A. Dey, Therapeutic strategies to overcome taxane resistance in cancer, Drug Resist. Updat. Rev. Comment. Antimicrob. Anticancer Chemother. 55 (2021), 100754.

[52] Y.H. Cheng, C. He, J.E. Riviere, N.A. Monteiro-Riviere, Z. Lin, Meta-analysis of nanoparticle delivery to tumors using a physiologically based pharmacokinetic modeling and simulation approach, ACS Nano 14 (2020) 3075–3095.

[53] E. Ahmadian, A. Eftekhari, H. Babaei, A.M. Nayebi, M.A. Eghbal, Anti-cancer effects of citalopram on hepatocellular carcinoma cells occur via cytochrome C release and the activation of NF-kB, Anti Cancer Agents Med. Chem. 17 (2017) 1570–1577.

[54] J. Qin, N. Gong, Z. Liao, S. Zhang, P. Timashev, S. Huo, X.-J. Liang, Recent progress in mitochondria-targeting-based nanotechnology for cancer treatment, Nanoscale 13 (2021) 7108–7118.

[55] H. Hou, X. Huang, G. Wei, F. Xu, Y. Wang, S. Zhou, Fenton reaction-assisted photodynamic therapy for cancer with multifunctional magnetic nanoparticles, ACS Appl. Mater. Interfaces 11 (2019) 29579–29592.

[56] A. Eftekhari, A. Arjmand, A. Asheghvatan, H. Švajdlenková, O. Šauša, H. Abiyev, E. Ahmadian, O. Smutok, R. Khalilov, T. Kavetskyy, M. Cucchiarini, The potential application of magnetic nanoparticles for liver fibrosis theranostics, Front. Chem. 9 (2021), 674786.

[57] E. Ahmadian, P.S. Pennefather, A. Eftekhari, R. Heidari, M.A. Eghbal, Role of renin-angiotensin system in liver diseases: an outline on the potential therapeutic points of intervention, Expet Rev. Gastroenterol. Hepatol. 10 (2016) 1279–1288.

[58] T. Wang, Q. Fan, J. Hong, Z. Chen, X. Zhou, J. Zhang, Y. Dai, H. Jiang, Z. Gu, Y. Cheng, Y. Li, Therapeutic nanoparticles from grape seed for modulating oxidative stress, Small Weinh. Bergstr. Ger. 17 (2021), e2102485.